universe

MDPI

Review

An Updated View of the Milky Way from Maser Astrometry

Katharina Immer [1,*,†] and Kazi L. J. Rygl [2,†]

[1] Leiden Observatory, Leiden University, P.O. Box 9513, 2300 RA Leiden, The Netherlands
[2] INAF-Istituto di Radioastronomia & Italian ALMA Regional Centre, Via P. Gobetti 101, I-40129 Bologna, Italy; kazi.rygl@inaf.it
* Correspondence: immer@strw.leidenuniv.nl
† These authors contributed equally to this work.

Abstract: Astrometric observations of maser sources in the Milky Way, using the Very Long Baseline Interferometry (VLBI) technique, have been exploited to determine the spiral structure of our Galaxy. Several major spiral arms have now been pinpointed in the first and second Galactic quadrants. Fundamental Galactic parameters such as the distance to the Galactic Centre and the rotation curve and speed have been determined. In this review, we discuss the latest results from the Bar and Spiral Structure Legacy survey, the VLBI Exploration of Radio Astrometry survey and other VLBI arrays and compare them with astrometric measurements of stars from the *Gaia* mission. In particular, we present the peculiarities of the individual spiral arms and a thorough discussion of the methods to determine different Galactic parameters as well as the obtained values.

Keywords: astronomical masers; astrometry; star formation; radio interferometry

Citation: Immer, K.; Rygl, K.L.J. An Updated View of the Milky Way from Maser Astrometry. *Universe* **2022**, *8*, 390. https://doi.org/10.3390/universe8080390

Academic Editors: Ciriaco Goddi, C. M. Violette Impellizzeri and Francisco Colomer

Received: 9 May 2022
Accepted: 19 July 2022
Published: 23 July 2022

1. Introduction

For almost a century, galaxies have been classified depending on their shape [1]. Reference [2], for example, identified our Galaxy as a barred spiral galaxy. However, due to the position of the Sun in the mid-plane of the Milky Way, disentangling the 3D structure of our Galaxy has been challenging so far. On the sky, the spiral arm features, located at different distances, are superimposed. Dust extinction increases significantly towards the centre of our Galaxy and beyond. In addition, distances are large which requires high astrometric precision (10 µas for a 10% accuracy at a distance of 10 kpc) to pinpoint objects within the spiral arms.

Natural targets to locate the spiral arms in our Galaxy are early-type stars and star-forming regions which are formed from the gas and dust reservoirs in the arms. The *Gaia* astrometry satellite has now measured accurate distances to almost 1.5 billion stars [3]. However, due to the dust extinction at optical wavelengths, measurements of targets in the Galactic plane are mostly limited to a few kpc from the Sun.

Observations at radio wavelengths, however, are not hindered by dust extinction. The necessary astrometric precision of 10 µas to locate objects even at the far side of our Galaxy requires the Very Long Baseline Interferometry (VLBI) technique. Due to the high angular resolution of these observations, targets need to be compact at mas levels and to show strong emission at radio wavelengths. Ideal objects for VLBI astrometry are maser sources in high-mass star-forming regions or around evolved stars as well as radio stars (see, for example, the Gould's Belt Distances Survey (GOBELINS) conducted with radio stars [4–8]. The types of masers targeted are hydroxyl (OH) masers at 1.6 GHz, Class II methanol (CH_3OH) masers at 6.7 and 12.2 GHz, water (H_2O) masers at 22 GHz, and silicon monoxide (SiO) masers at 43 GHz. Maser emission arises in the direct surroundings of young forming stars as well as evolved stars, pumped by either strong infrared emission or violent collisions in disks, outflows, or winds and traces the internal kinematics of their host stellar systems. The different excitation mechanisms lead to variability in the

maser emission, often on timescales shorter than a year. This requires a higher cadence of observations for certain types of masers (H_2O, SiO).

In particular, maser astrometry of high-mass star-forming regions is very effective at tracing spiral structure, because high-mass star-forming regions are located mostly in the spiral arms. Thanks to their strong emission they are bright enough to be detected even from the far side of the Galaxy. Several VLBI astrometry projects [9,10] over the past decade have targeted maser-bearing high-mass star-forming regions to define the Galactic plane and the position of the Sun relative to it. This yields the orientation of the plane as well as the vertical distance of the Sun to it.

Together with the parallax, the proper motion of the masers is determined. To infer the proper motion of the host system it should be taken into account that maser sources also trace internal motions, especially for collisionally pumped maser species in winds and outflows. These internal motions can be of the order of a few to tens of km s^{-1} for methanol and water masers, respectively [11–14]. Combining the proper motions with line-of-sight velocities, distances and positions yields the full 6D space information of the star-forming regions. These results have been fitted with simple rotation curves to determine the distance to the Galactic Centre as well as the 3D motion of the Sun on its orbit around it.

In this review, we summarise the conducted observations with different VLBI arrays in Section 2 and the applied calibration techniques in Section 3. A short summary of the obtained *Gaia* results in comparison with the VLBI results is given in Section 4. We present the spiral arm structure of the Milky Way as well as peculiarities of the individual spiral arms in Sections 5 and 6. We proceed with a discussion of the fundamental Galactic parameters in Section 7 before ending with a summary and an outlook to the future in Section 8.

2. Observations and Data Calibration

2.1. BeSSeL VLBA Observations and Data Calibration

The Bar and Spiral Structure Legacy (BeSSeL) survey[1] [15] is a key science project of the Very Long Baseline Array (VLBA). The VLBA consists of ten 25-m antennas with a maximum baseline of 8611 km. The BeSSeL observations covered the 6.7 and 12.2 GHz methanol maser transitions as well as the 22.2 GHz water maser transition. The methanol masers were observed for four epochs, spread over one year to optimally sample the minima and maxima of the parallax signature in right ascension and minimize the correlation of the parallax and proper motion signatures. Since water maser features often have life times of less than a year, they were targeted in six epochs to ensure parallax measurements for water maser features that were detected over at least seven months. Distant source candidates were visited in 16 epochs to trace well the small parallax signature.

Together with each maser target, observations of two to four position reference sources were conducted as well. Accurate positions of these extragalactic background sources were determined in a preparatory survey with the VLBA [16]. The phase-referencing calibration was conducted on the maser targets since they were always brighter than the background sources. The full calibration of the data sets is described in detail in [17].

Three to four "geodetic" observing blocks were placed at the beginning, in the middle and at the end of the phase-referencing observations. The blocks allowed the BeSSeL team to monitor slow changes in the atmospheric delay at each telescope by observing a number of bright extragalactic sources with well-determined positions over a large range of azimuths and elevations [18]. Ionospheric effects were calibrated by removing an estimate of the dispersive delay based on global models of the total electron content of the ionosphere derived from Global Positioning System (GPS) data [19]. For the 12 GHz methanol and 22 GHz water masers, this approach was sufficient. However, at 6.7 GHz observing frequency, residual dispersive path-delays from this method can be a limiting factor in determining parallaxes beyond 1 kpc. Uncompensated dispersive delays can lead to systematic errors in the relative position between maser and quasar at each epoch,

which in turn can lead to measured parallax gradients on the sky. Reference [20] developed a method to mitigate these effects (see Section 3.1 for a short description and [20,21] for more details).

The BeSSeL data were reduced using the NRAO's Astronomical Image Processing System (AIPS; [22]) and ParselTongue [23].

2.2. VERA Observations and Data Calibration

The VLBI Exploration of Radio Astrometry[2] (VERA) array consists of four 20-m antennas located across Japan, yielding baseline lengths between 1020 to 2270 km. VERA maser astrometry observations are performed using the 22.2 GHz water maser transition and, less frequently, the SiO transitions at 43.1 GHz and 42.8 GHz, respectively. The maser targets observed for astrometry were low- and high-mass star-forming regions, red super giants and asymptotic giant branch stars. Typically, the maser target was observed for one year with a cadence of 1 to 2 months to track the varying maser features and sample the parallax ellipse sufficiently. Some targets were monitored for even two or more years, and the more variable targets had a higher cadence.

VERA antennas have a dual-beam receiver system that permits to track a maser target and phase reference source pair simultaneously [24]. Phase reference sources were selected from the VLBA Calibrator Catalogue [25] or from VERA calibrator observations [26,27]. Bandpass and delay calibrators were observed every 60–80 min. Amplitude calibrations were performed through the chopper-wheel method [28]. The typical frequency setup consisted of 16 spectral windows of 16 MHz bandwidth each. One of the spectral windows was centred on the maser target using a high spectral resolution of 15.625 kHz or 31.25 kHz, while the remaining spectral windows were used for recording continuum emission of the phase reference source.

The observations were corrected for tropospheric and ionospheric delays based on GPS measurements and meteorological data [29]. Further VERA-specific corrections included a path length correction, to remove differences in path lengths for the maser and phase reference targets, which were determined by inserting an artificial noise source in the observed signal (see [24] for more details). Instrumental delays and phase offsets between spectral windows were corrected by fringe fitting a bright calibrator source. Phase and delay solutions were determined on the phase reference calibrator and applied to the maser target. For weak phase reference sources, the inverse phase calibration method was implemented, fringe fitting a bright maser channel and applying the solutions to the phase reference source. Both methods deliver relative maser-phase reference source positions necessary for parallax and proper motion astrometry.

VERA data calibration was performed using AIPS [22] and the VEra Data Analyzer (VEDA) package [30].

2.3. Astrometric Observations with Other Telescopes

2.3.1. The European VLBI Network

References [31,32] measured the first 6.7 GHz methanol maser parallaxes. This transition is particularly interesting to explore for astrometry because it is brighter and more ubiquitous than the 12.2 GHz methanol maser emission and found to be exclusively associated with high-mass star-forming regions [33]. In addition, due the lower frequency, in particular with respect to the 22.2 GHz water maser transition, less tropospheric delay is expected.

Both of these observations were performed with the European VLBI Network (EVN), constituting the first maser parallaxes obtained with the EVN. The longest baselines were about 9000 km and the largest antenna in the array was the Effelsberg 100-m antenna. While the [31] observations targeted a set of high-mass star-forming regions at different Galactic longitudes using five epochs, the second astrometric observations of [32] used eight epochs and targeted a number of high-mass star-forming regions in the Cygnus X complex. This allowed [32] to optimise the scheduling so that the observing epochs were close to the

minima and maxima of the parallax signature in right ascension because of the common Galactic longitude.

During an EVN observing run, the astrometric observations were interleaved with geodetic-like observing blocks to calibrate the tropospheric zenith delays at each antenna [17,18,34]. The maser targets were observed in a cycle with one or two nearby position reference sources found from the VLBA calibrator catalog [25,35–38], from [39] or by doing VLBI observations to check the compactness of point-like, nearby NVSS [40] sources.

The EVN observations were recorded at a rate of 512 Mbps and correlated twice at the Joint Institute for VLBI-ERIC (JIVE), creating "continuum" and "spectral line" data sets. The continuum data set used eight spectral windows of 8 MHz in dual polarization with a channel spacing of 0.25 MHz. The spectral line data set consisted of only one 8 MHz spectral window, but with a much finer channelisation of 7.81 kHz.

The calibration followed the EVN guidelines applying the parallactic angle correction, and using the ionospheric corrections from the Jet Propulsion Laboratory (JPL) GPS–IONEX total vertical electron content maps of the atmosphere. Earth Orientation Parameters were already corrected at the JIVE correlator. The tropospheric delays were applied from the, separately analysed, geodectic block observations. System temperature measurements and gaincurves were used to perform the amplitude calibration. Spectral window phase and delay offsets were calibrated on a bright calibrator target. The data were calibrated via inverse phase referencing by fringe fitting a bright maser channel and applying the solutions to the maser data and to the continuum data of the position reference sources.

The EVN data calibration was performed using AIPS [22] and ParselTongue [23]. The best parallax uncertainty reached in the EVN observations at 6.7 GHz is 22 μas [31].

The maser astrometry results from the EVN observations were included in the BeSSeL survey [9,41].

2.3.2. The Australian Long Baseline Array

Reference [42] published the first parallax results of the Long Baseline Array (LBA) in Australia. They targeted the 6.7 GHz methanol maser transition towards the source G339.884−1.259. For these observations, the LBA was comprised of the Ceduna 30-m antenna, the Hartebeesthoek 26-m antenna, the Hobart 26-m antenna, the Mopra 22-m antenna, the Parkes 64-m antenna and the Australia Telescope Compact Array (ATCA). Either four or five of the 22-m ATCA antennas were phased and combined.

The observations were conducted in two frequency configurations, one for the calibration of the tropospheric delay and one for the phase referenced maser observations. Several geodetic blocks were included in the observations to determine the troposphere path length contributions and model the clock drift rates at each telescope.

The data calibration steps were based on [17]. First, the ionospheric delay, Earth Orientation Parameter and parallactic angle effects were calibrated and removed before corrections for the troposphere and clock drift rate were applied. Afterwards, an amplitude calibration was conducted based on a single autocorrelation scan from the Parkes telescope to which all the other antennas were scaled using the nominal system equivalent flux density values of the antennas. A single scan on the phase calibrator was used to correct the initial residual clock and instrumental errors. Since the continuum and maser data were not observed with the same spectral resolution, the solutions were modified accordingly before applying them to the maser data.

The best suited maser channel for inverse phase-referencing was identified from the cross-correlation spectra, showing the smallest relative flux density variations across all baselines during the observations. The maser coordinates were iteratively changed until there was no further improvement in the position of the continuum source towards the centre of the image.

The maser astrometry results from the Australian LBA observations were included in the BeSSeL survey [9].

3. Determination of Parallax and Proper Motion

3.1. BeSSeL Maser Parallax and Proper Motion Determination

To obtain the positional data of the maser targets and the background quasars per epoch, the sources were imaged and elliptical Gaussian brightness distribution models fitted to the brightest maser spots and the continuum sources. The relative position offsets between maser spots and background sources were modelled with a sinusoidal parallax in combination with linear proper motion components in right ascension and declination. The ellipticity of the Earth's orbit was included in the model [17].

Every maser spot with compact emission and minimal blending was tested for its astrometry quality by fitting a parallax and proper motion model and assessing the magnitude of the post-fit residuals. Usable maser spots were then combined in one parallax fit together with all usable background continuum sources. To take internal motions in the star-forming regions into account, individual maser spots were allowed to have different proper motions in the combined fit but they were constrained to be the same for an individual maser spot if measured against different background continuum sources. If N maser spots were used in the combined fit, the uncertainty of the parallax was increased by a factor of $\sqrt{(N)}$, making the conservative assumption that the positional uncertainties of the maser data are 100% correlated.

Since the position uncertainties from the brightness distribution fitting were often unrealistically small, the BeSSeL team added independent error floors in quadrature to these position uncertainties for the right ascension and declination position data to account for systematic errors such as unmodelled atmospheric delays. These error floors were then adjusted until the reduced χ^2 of the parallax and proper motion fit was close to unity in each coordinate [17]. Potential internal motions of the masers with respect to the young stellar object (YSO) were taken into account by adding, in quadrature, 5 and 10 km s^{-1} to the proper motion uncertainties of the 6.7 GHz methanol and 22 GHz water masers, respectively. The best parallax uncertainty of 5 µas was reached by [43] for a 22 GHz water maser in G048.60+0.02.

As mentioned in Section 2.1, gradients in the fitted parallax value were found for 6.7 GHz methanol maser targets which were attributed to uncompensated dispersive delays from the ionosphere. Reference [20] developed the following method to mitigate these effects. First, the relative position data of the background quasars was used to produce position data for an "artificial" quasar at the position of the 6.7 GHz target maser and then the parallax and proper motion measurements were conducted between the maser and the artificial quasar. This method is based on the MultiView approach described in [44] and improves the parallax accuracy significantly. However, it yields poor estimates of the parallax uncertainty. Reference [21] further developed this method by fitting the positional data of the maser relative to the background quasars at each epoch as the sum of the parallax and proper motion signature as well as a planar tilt of the quasar positions relative to the maser position (due to the unmodelled ionospheric effects). This approach improved the parallax uncertainty estimate. The best 6.7 GHz methanol maser parallax uncertainty was 13 μas, obtained by [21].

3.2. VERA Maser Parallax and Proper Motion Determination

After imaging the maser and phase reference targets, the maser spot and phase reference source positions were determined by 2D Gaussian fitting routines. Relative maser–phase reference position offsets in right ascension and declination were fitted with a sinusoidal parallax signature and linear proper motions in right ascension and declination. The atmospheric path length errors affect the astrometric accuracy in declination stronger than in right ascension. Therefore, when the accuracy in declination was significantly worse than in right ascension, only the right ascension data were used for the parallax determination. Similarly to the BeSSeL programme, uncertainties of the best-fitting parameters were estimated by adding error floors to all the astrometry data to obtain a fit with reduced

χ^2 equal to unity [17]. These additional error floors were regarded as a sum of systematic, mostly residual atmospheric delays, and random thermal errors.

For maser targets with multiple maser features, the VERA survey used two approaches: (1) all individual features were fitted simultaneously with one parallax value but allowing individual proper motions for each maser feature; (2) each maser feature was fitted individually for a parallax and a proper motion after which all results were averaged to obtain the final results. In the latter case, the standard deviation of the maser parallaxes was quoted as the parallax uncertainty. The best parallax uncertainty of 7 µas was reached by [45] for a 22 GHz water maser in G048.61+0.02. Possible internal motions of the maser emission with respect to the central YSO were not taken into account in the quoted proper motion uncertainties. To calculate 3D velocities, the VERA programme used Local Standard of Rest (LSR) velocities from ammonia or CO molecular line catalogues or the masers themselves (using a 5 km s^{-1} uncertainty).

A comparison of 28 VLBA/EVN and VERA parallaxes finds that for a large majority of maser targets (21 out of 28) the parallaxes agree within 2σ joint error ([21], where the parallax of [10] was used for W 48). The mean and the standard deviation of the parallax difference are -0.002 and 0.318 mas, respectively, for the sample of 28 targets.

3.3. Distance Determination from Absolute Proper Motion Measurements

This method was developed by [46]. It assumes that all stars are located in the Galactic plane and follow circular orbits around the Galactic Centre. The proper motion of a star in direction of longitude is a function of the distance to the star and the tangential velocity which in turn is a function of the distance to the Galactic Centre, the distance to the star, the longitude of the star, the rotation speed of the Sun and the rotation speed of the star. Assuming a Galactic rotation curve and measuring the absolute proper motion of the star thus provides a method to determine the distance to the star (see [46,47], for more details).

Reference [46] points out that the distance uncertainty for the proper-motion method is the smallest along the line between the Sun and the Galactic Centre and the largest around the tangent point circle.

This method was applied by [47] who measured a distance of 20 kpc for G7.47 + 0.06. This result was later confirmed by [48] via direct parallax measurements. The consistency between the two measurements is a great demonstration of the validity of this method (see Section 6.6 for more details).

3.4. Distances through the Phase-Lag Method

Variable OH/IR stars are evolved stars experiencing a high mass-loss which has resulted in an optically thick circumstellar envelope or shell with strong 1612 MHz OH maser emission. The OH maser emission is pumped radiatively by the infrared emission of the warm dust in the shell. The maser variability originates in the brightness pulsations of the evolved star. The strongest maser emission arises in the front and back central caps of the shell, where there is the largest velocity coherence along the line-of-sight thus increasing the maser brightness. Spectra of variable OH/IR stars show typically a blue-shifted and red-shifted maser peak, through which the emission from the front and back cap, respectively, can be identified.

The phase-lag method is based on the determination of the time lag between the front and back cap for obtaining the linear diameter of the shell [49] and combines this with VLBI maser imaging to obtain an accurate angular diameter of the shell from which the distance can then be calculated [50]. The time lag determination requires long-term (one to six years) single dish maser monitoring to obtain a light-curve covering at least a full period. The VLBI observations require high sensitivity as the maser emission on the edge of the shell (as seen from our line-of-sight) will be weaker due to lesser velocity coherence for these regions.

The phase-lag method can achieve distance uncertainties of 20% up to distances of about 5 kpc [51]. OH maser parallax measurements of evolved stars [52] can also achieve

such uncertainties, however all the successful measurements have been for more close by, within 2 kpc, objects so far. Other distance methods are not viable for these objects: *Gaia* parallaxes are impossible due to the optically thick circumstellar envelope, period-luminosity relations are not valid for these stars because of their long periods [53], and kinematic distances are not reliable due to high peculiar motions [54].

The phase-lag method is thus important to obtaining distances for the more distant evolved stars.

4. Comparison with *Gaia* Astrometry

The *Gaia* catalogue is published in various Data Releases (DR) as more information is being collected by the satellite and analysed. At the time of writing, DR3 [55] had just been released[3]. In *Gaia* DR3, the best parallax uncertainty reached for O-type stars is 10 μas, comparable to the maser VLBI parallax uncertainties.

Reference [56] performed a comparison of VLBI (maser and continuum VLBI) and *Gaia* DR2 [57] astrometry for a sample of 93 stars that have both VLBI and *Gaia* astrometric measurements. This sample included 59 YSOs, 19 Asymptotic Giant Branch (AGB) stars, and 15 other radio stars (for example, low-mass stars, cataclysmic binaries, high-mass X-ray binaries and long-period variable stars). The AGB and YSO subclasses were further divided into binaries and non-binaries. The authors calculated the slope and intercept for the VLBI and *Gaia parallaxes* of each subclass and combined samples, for the sample including binaries and without. For each stellar subclass and also for their full data set [56] found that VLBI and *Gaia* DR2 parallaxes have slopes of unity within 2σ. Per subclass they measured the following slopes: AGBs: 1.008 ± 0.080 and 1.069 ± 0.078 when removing binaries; YSOs: 0.999 ± 0.010 and 0.985 ± 0.012 when removing binaries; other radio stars: 1.004 ± 0.003. Clearly, AGB stars have larger uncertainties with respect to the other classes. The intercepts have a small, negative value implying that *Gaia* DR2 parallaxes are systematically smaller than VLBI parallaxes. These results show that the VLBI and *Gaia* results are in good agreement on average, but that AGB stars are more prone to discrepant astrometry and that there is a zero-point offset for the *Gaia* DR2 data. In fact, [58,59] found notable differences between VLBI and *Gaia* results for AGB stars. These authors suggest that the asymmetric structure and the brightness fluctuations of those stars lead to a variation of their photo centre positions which causes a systematic error in the *Gaia* parallax.

After removing the AGB stars and the binary stars (because the unmodelled orbital motion of these objects can cause unreliable parallaxes), [56] determined the *Gaia* DR2 zero-point offset to be -75 ± 29 μas. This is a bit larger than the value presented for faint quasars of -29 μas by [60] and more similar to the values presented for the (optically) brighter stars of about -50 μas (see [61–63] for references).

Reference [64] compared the local spiral structure from *Gaia* Early Data Release 3 ([3], EDR3]) astrometry of O-type stars, i.e., stars with the shortest main sequence lifetimes between 1 and 8 Myr [65] and that are expected to be located close to their birth sites, with the BeSSeL maser parallaxes [9]. The spiral structure emerging from O-star and maser astrometry appears similar within the $\sim$3 kpc region around the Sun in which reliable (better than 10% uncertainty) *Gaia* distances are possible. From Figure 2 in [64], it is clear that O-stars trace the spiral arms but not as precisely as maser-bearing SFRs as the O-star distribution is more scattered and a number of O-stars appear to be present in the inter-arm regions. Reference [64] interprets this finding as an indication for some high-mass star formation occurring possibly in the inter-arm regions or potential migration of O-type stars from their birth sites in the spiral arms. However, the latter would require unusually high peculiar motions for these objects [66].

As there is a larger number of O-stars with *Gaia* astrometry than maser targets with VLBI astrometry, in particular in the third and fourth Galactic quadrants, *Gaia* astrometry is particularly important for extending the spiral arm tracing in these quadrants. Presently, these quadrants have few targets with maser astrometry due to the low declination of these regions requiring a Southern Hemisphere VLBI array such as the LBA.

5. Spiral Arm Structure of the Milky Way

Maser astrometry delivers accurate positions, parallaxes and proper motions. These, together with the radial velocity of the maser star, taken from typical high-density tracing molecules such as NH_3, CS or CO, can be used to obtain 3D positions (X, Y, Z) and 3D motions (U; motion toward the Galactic Centre, V; motion in the direction of Galactic rotation, W; motion toward the north Galactic pole). Figure 1 shows the orientation of these motion components. Since maser stars in high-mass star-forming regions trace the Galactic plane well, one can use them as markers to fit a Galactic rotation curve (see Section 7).

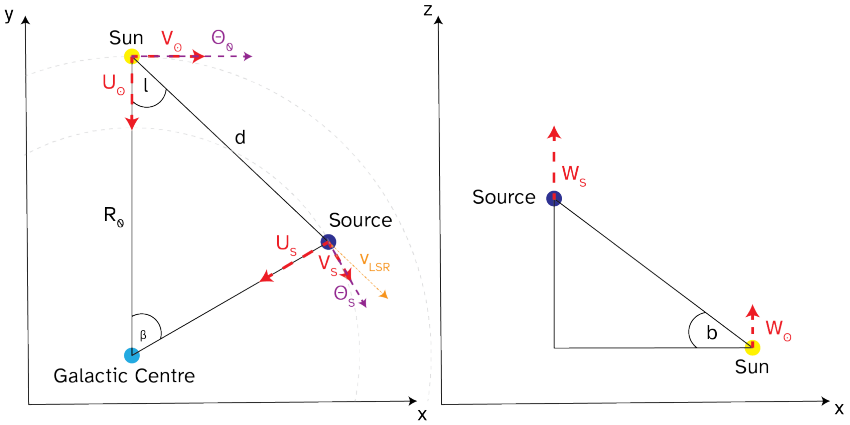

Figure 1. Sketch of the Solar and source parameters with a depiction of the distance to the Galactic Centre R_0, the distance d to the source, the azimuth β, the 3D motions of the Sun ($U_\odot$, $V_\odot$, $W_\odot$) and the source (U_S, V_S, W_S), the line-of-sight velocity of the source v_{LSR} and the rotation speeds Θ_0 and Θ_S at the positions of the Sun and the source, respectively.

5.1. Arm Assignment

Large-scale observations of HI and CO (e.g., [67–70]) show quasi-continuous emission features in longitude-velocity (l-v) space which can be identified as spiral arms. The density of molecular clouds in the interarm regions is much smaller than in the spiral arms. Locating those spirals arms in a plan view of the Milky Way by transforming velocity to (kinematic) distance can be error-prone due to near-far distance ambiguities and large peculiar motions in some spiral arms.

Maser sources in high-mass star-forming regions can be assigned to spiral arms by associating them with molecular clouds. This requires a good agreement of the position and line-of-sight velocity of the maser with the (l-v) locus of the arm (see Figure 3 in [9]). For objects with uncertain spiral arm assignment based on their line-of-sight velocities alone, additionally their proper motion and parallax are used in the updated version of the parallax-based distance calculator[4] [9,71] for their localisation in the Milky Way.

5.2. Spiral Arm Model

After the assignment of the maser sources to spiral arms, the spiral arm structure becomes evident when the maser sources are plotted in a plan view of the Milky Way (see Figure 2). The figure shows that the maser sources trace continuous features with only a few sources in the regions between the spiral arms. Combining the radial and azimuthal locations of the masers with their measured distances, one can fit spiral arm patterns to these features. An ideal log-periodic spiral is defined by

$$\ln\left(\frac{R}{R_{\rm ref}}\right) = -(\beta - \beta_{\rm ref}) \tan\psi, \quad (1)$$

where R is the Galactocentric radius at azimuth β for a spiral arm with radius $R_{\rm ref}$ at reference azimuth $\beta_{\rm ref}$. The azimuth β is defined as 0 towards the Sun and increases with Galactic longitude (see also Figure 1). The pitch angle ψ is the angle between the spiral arm

and a tangent to a Galactocentric circle at the same radius [54]. A study of spiral galaxies by [72] showed that spiral arms consist of arm segments with a typical length of 5−8 kpc, separated by a kink (i.e., an abrupt change of the pitch angle from one side of the kink to the other) or gaps. Allowing for one kink over the typical length of the traced spiral arms, (Figure 2) the formula is adapted to:

$$\ln(\frac{R}{R_{\rm kink}}) = -(\beta - \beta_{\rm kink}) \tan \psi, \quad (2)$$

where $R_{\rm kink}$ is the Galactocentric radius at azimuth $\beta_{\rm kink}$ where the abrupt change in pitch angle occurs [9]. Plotting the logarithm of the Galactocentric radius against azimuth, the spiral arm segment can be fitted with a straight line where the slope of the line is proportional to the tangent of the pitch angle. The perpendicular separation of the maser sources from the fitted line was minimized with a Bayesian fitting procedure. Deviations from the logarithmic model are expected for spiral arm segments with an intrinsic width of several hundred parsecs. The arm width can be estimated by including it as a noise term in quadrature with the parallax uncertainty when fitting for the pitch angle (for more details about the arm fitting see [9,41]). References [9,41] found that the spiral arm width increases linearly with Galactocentric radius at a rate of 36 pc kpc^{-1}.

The fitted pitch angles and arm widths are summarised in Table 1 for each of the spiral arms. The kinks and pitch angles of each arm are discussed in detail in [9]. The size of the fitted maser sample as well as the covered azimuth range can have a large effect on the pitch angle. Within overlapping azimuth ranges, the pitch angles of the global fits for each of the arms agree within their joint uncertainties. However, larger sample sizes and azimuth ranges facilitate splitting the spiral arm into smaller sections or fit the arm with a kink which can result in different pitch angles compared to the global fit. Increasing the azimuth coverage of the maser sample for each of the arms in the future, especially into quadrant 4, will contribute to uncovering a more detailed picture of the spiral arms.

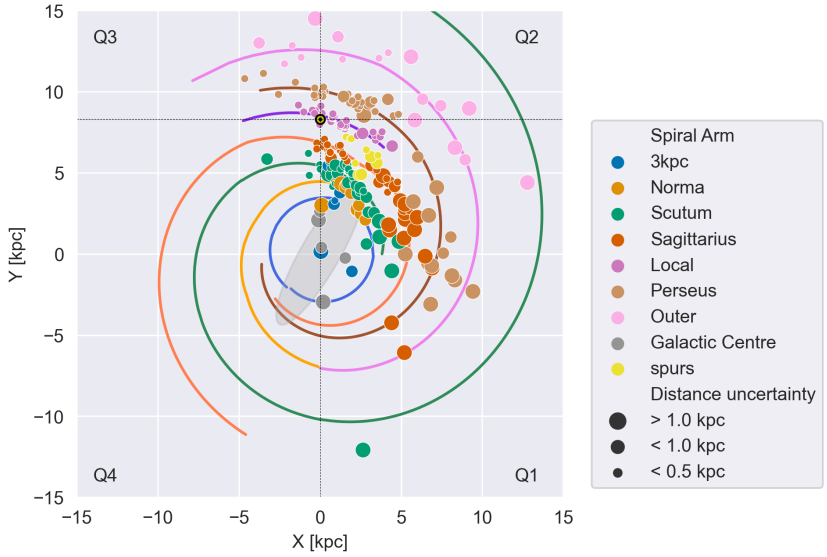

Figure 2. A plan view of the Milky Way as seen from the north Galactic pole. High-mass star-forming regions with maser parallax measurements from the BeSSeL survey [9,73] and VERA survey [10] are marked; the colour of the markers denotes the spiral arm association; the size of the marker corresponds to the mean distance uncertainty in kpc; also shown are spiral arms from [9], coloured by spiral arm or by source grouping (Galactic Centre, spurs), and the Galactic "long" bar from [74] as a grey filled ellipse. The Galactic Centre is located at the origin of the plot, the Sun, shown by a Sun symbol, at (0, 8.15). Galactic quadrants are named and indicated by dashed lines.

Table 1. Pitch angles, widths and average peculiar motions of the different spiral arms, measured for different numbers of sources N_S. The rows with entries for multiple pitch angles refer to fits which include a kink at Galactic azimuth β_{kink} (given in the comments column); the first pitch angle is for azimuth $\beta < \beta_{kink}$, the second pitch angle for azimuth values $\beta > \beta_{kink}$; see Section 5.2 for details. When data other than maser VLBI astrometry were used in the pitch angle fitting, it is indicated in the comments column [75–95].

Arm	Pitch Angle 1 (deg)	Pitch Angle 2 (deg)	Width (kpc)	$\overline{U}_S$ (km s^{-1})	$\overline{V}_S$ (km s^{-1})	$\overline{W}_S$ (km s^{-1})	N_S	Reference	Comment
Outer	14.9 ± 2.7			1.8 ± 2.9	-3.3 ± 4.4	11.7 ± 2.3	6	[76]	
	3.0 ± 4.4	9.4 ± 4.0	0.65 ± 0.16				11	[9]	$\beta_{kink} = 15°$
	11.5 ± 1.9						15	[85]	+ young star clusters
Perseus	17.8 ± 1.7						8	[95]	
	14.8 ± 0.8						14	[85]	
	9.9 ± 1.5			9.4 ± 1.3	-4.4 ± 2.0	-2.1 ± 1.1	25	[81]	
	9.2 ± 1.5		0.39				27	[82]	
	10.3 ± 1.4	8.7 ± 2.7	0.35 ± 0.06				41	[9]	$\beta_{kink} = 40°$
Inner	5 ± 4			-8.4 ± 2.5	-9.7 ± 8.3	2.6 ± 2.8	9	[80]	$l = 30° - 50°$
Outer				14.1 ± 1.4	-7.6 ± 1.4	-1.7 ± 1.3	16	[80]	$l = 90° - 140°$
				3.5 ± 1.8	-3.3 ± 2.0	-1.2 ± 1.9	9	[80]	$l = 170° - 245°$
Local	10.1 ± 2.7			1.3 ± 1.3	-5.4 ± 1.0	2.4 ± 1.4	30	[87]	
	11.6 ± 1.8						38	[86]	
	11.4 ± 1.9		0.31 ± 0.05				28	[9]	
Sagittarius	7.3 ± 1.5		0.21	2.9 ± 1.5	3.7 ± 1.5	-1.7 ± 1.4	18	[89]	
	9.3 ± 2.2						7	[85]	
	17.1 ± 1.6	1.0 ± 2.1	0.27 ± 0.04				35	[9]	$\beta_{kink} = 24°$
Global	7.2 ± 1.9			2.6 ± 1.1	4.5 ± 1.3	-0.7 ± 1.1	30	[21]	
Near	9.4 ± 3.9			2.0 ± 1.4	7.1 ± 1.5	-1.1 ± 1.5	12	[21]	$l = 351° - 50°$
Far	5.4 ± 3.3			4.3 ± 2.4	-0.6 ± 2.2	2.0 ± 1.4	18	[21]	$l = 32° - 52°$
Scutum	19.8 ± 3.1		0.17	8.2 ± 2.3	-4.2 ± 2.6	-1.5 ± 1.5	16	[92]	
	11.2 ± 4.0						4	[85]	
	14.1 ± 1.7	12.1 ± 2.4	0.23 ± 0.05				36	[9]	$\beta_{kink} = 23°$

6. Individual Spiral Arms

In this section, we will discuss the peculiarities of each spiral arm.

6.1. Outer

The Outer spiral arm, the second spiral arm from the Sun towards the Galactic anticentre, possibly connects to the Norma spiral arm at the far side of the Milky Way (see discussion in [9], and the plan view of the Milky Way in Figure 2). The star formation activity in the outer segments of this arm is relatively low (see Figure 3). So far, parallaxes to 17 sources have been measured.

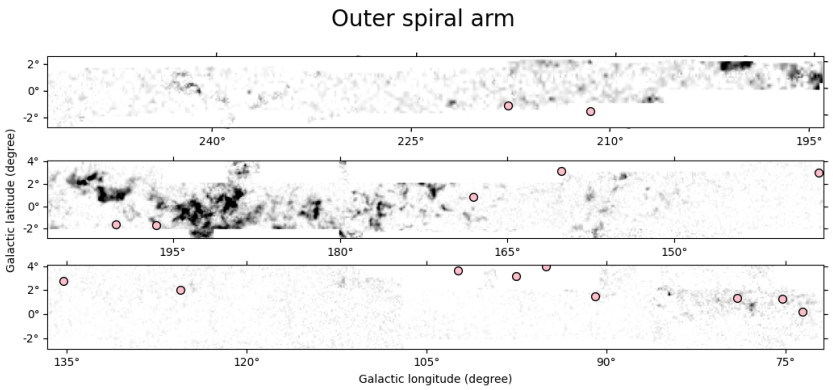

Figure 3. The Outer spiral arm maser parallax sources (pink dots) overplotted on the second and third quadrant CO data from [70,75] integrated within ± 20 km s^{-1} from the LSR velocities obtained by [9].

The Galaxy warps towards the north Galactic pole in quadrants 1 and 2 and towards the south Galactic pole in quadrants 3 and 4. A signature of this warp is that the sources assigned to the Outer arm are mostly located above the Galactic plane (Figure 3). With the current parallax measurements, the warp can be traced between $Z = 200{\sim}600$ pc over a longitude range of $75^\circ < l < 183^\circ$ [76,77]. The structure of the Z-height is discussed in more detail in Section 7.3.

Most sources with Galactocentric distance beyond 7 kpc have peculiar motion values towards the north Galactic pole that are consistent with or close to zero [9,77]. This indicates that the Outer arm sources are also mostly moving in the Galactic plane.

6.2. Perseus

The Perseus arm is thought to originate near the far end of the Galactic bar from where it wraps through the inner Galaxy in the fourth and first quadrants and then the outer Galaxy in the second and third quadrants (Figure 2). Reference [43] found that there is a significant gap of 22 GHz water maser candidates between Galactic longitudes of 50° and 80° (Figure 4). Similarly, the number of massive young stellar objects in the Red MSX Source (RMS) survey [78] is low in this longitude range and the CO emission between longitudes of 64° and 76° is weak ([43,70], Figure 4). The density of HII regions in the catalog of [79] in this part of the Perseus arm is also much lower than in other parts [80]. This lack of star-forming regions suggests low levels of star formation over an extended period of time in this part of the Perseus arm which is in support of theoretical considerations regarding the formation of spiral arms in segments.

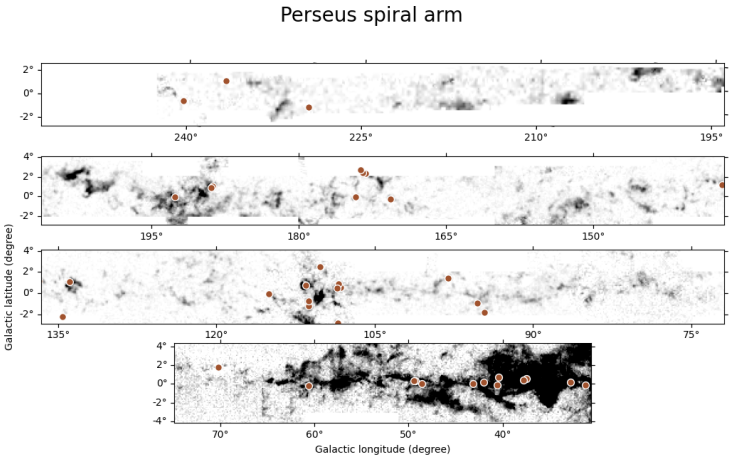

Figure 4. The Perseus spiral arm maser parallax sources (brown dots) overplotted on the first, second and third quadrant CO data from [70,75] integrated within ± 20 km s^{-1} from the LSR velocities obtained by [9].

Measuring the peculiar motions, [81] found that the masers in the Perseus arm, on average, move towards the Galactic Centre and slower than on circular orbits. Reference [80] investigated the peculiar motions of masers in the inner ($30^\circ < l < 50^\circ$) and outer ($l > 90^\circ$) Perseus arm segments and found a significant difference in the average motion towards the Galactic Centre. While the outer Perseus arm sources in quadrant 2 display significant motions, on average, towards the Galactic Centre, the inner arm sources in quadrant 1 show only modest motions in the U component. They conclude that the Perseus arm is not a single coherent feature since the different segments seem to be moving away from each other and thus might be independent.

Reference [82] separated the outer arm segment of the Perseus arm into an interior, middle and exterior section and compared the average peculiar motion for each of these sections. For the interior section, they found a radially inward motion while the middle section showed a marginal detection of motion slower than Galactic rotation. The exterior of the arm did not exhibit any statistically significant peculiar motion. They conclude that

these findings are consistent with formation models of spiral arms that predict gas entering an arm, being shocked and then forming stars (see for example [83,84]). They executed a similar experiment for the Local and Sagittarius arms but could not find a clear pattern among the arms.

6.3. Local

There has been a long debate about whether the Local arm is a secondary spiral feature or a major spiral arm. Maser parallax observations showed that many star-forming regions that were thought to be located in the Perseus arm based on their kinematic distance are actually located in the Local arm.

This arm is very actively forming stars (Figure 5). It has a length of more than 5.5 kpc and a width of 0.31 kpc, consistent with the trend seen in other spiral arms [9]. The Sun is located close to the inner edge of the arm. At the position of the Sun, the Local arm is located closer to the Perseus than the Sagittarius arm, at separations of 1.5 and 2 kpc, respectively. Reference [85] showed that there is no significant difference in pitch angle for low- and high-mass stars in the arm.

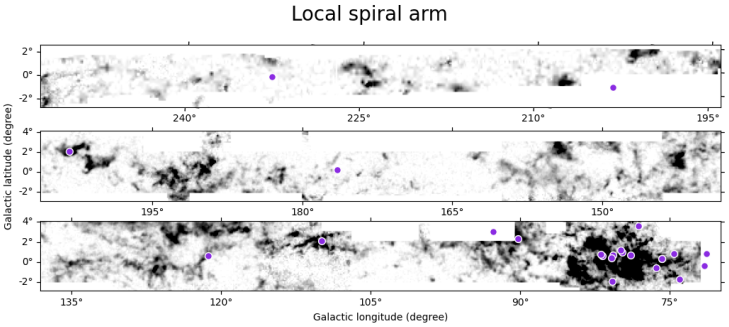

Figure 5. The Local spiral arm maser parallax sources (purple dots) overplotted on the second and third quadrant CO data from [70,75] integrated within ± 15 km s^{-1} from the LSR velocities obtained by [9].

At a Galactic longitude of 50°, a spur with a high inclination seems to bridge the Local and Sagittarius arms, traced by six star-forming regions with maser parallax measurements as well as large-scale molecular emission from CO [70,86].

Reference [87] provided three possible origins for the Local arm:

- a branch of the Perseus arm with a bifurcation point at a distance of 6 kpc at a Galactic longitude of 55° which is supported by the vicinity of the Local to the Perseus arm and by the fact that branches often branch off at the inner edge of an arm;
- a branch of the Carina–Sagittarius arm with a bifurcation point at a longitude of 282° which yet has to be confirmed with maser parallax measurements from the Southern Hemisphere;
- an independent spiral arm segment which is contradictory to the theory of spiral density waves [88] due to the small distances to the adjacent spiral arms.

6.4. Sagittarius

The Sagittarius arm is the first spiral arm from the Sun towards the Galactic Centre. The closest section of the arm has a distance of 1.4 ± 0.2 kpc from the Sun [89]. The high-mass star-forming regions in the far side of the arm in the first quadrant, beyond the tangent point, are located on average 15 pc below the IAU-defined Galactic midplane [21], Figure 6. The masers in this arm do not show any large peculiar motions (>20 km s^{-1}), but the sources in the near side of the arm have a small average motion in the direction of Galactic rotation [21,89].

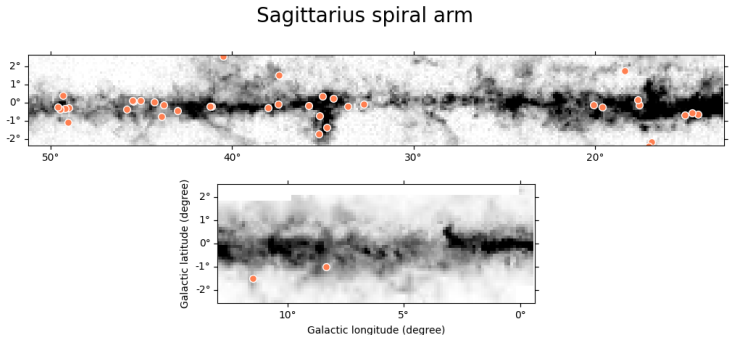

Figure 6. The Sagittarius spiral arm maser parallax sources (orange dots) overplotted on the first quadrant CO data from [70,90] integrated within ± 15 km s^{-1} from the LSR velocities obtained by [9].

6.5. Scutum

The Scutum spiral arm is the second arm from the Sun towards the Galactic Centre. Figure 7 shows the distribution of the star-forming regions with maser astrometry in the Galactic plane. Many high-mass star-forming regions associated with this arm are located close to the near end of the Galactic bar ($l \sim 30°$, Figure 2) [91–93]. Reference [92] fitted a large pitch angle of $19.8 \pm 3.1°$ to 16 sources in this arm. They argue that this large pitch angle might be caused by the vicinity of the Galactic bar. Reference [94] showed for external galaxies and in models that the bar of a spiral galaxy can bias the pitch angle at inner radii to larger values compared to the global pitch angle of the spiral arms. However, a more recent spiral arm fit of 36 sources in this arm from [9] yields a pitch angle of $13 \pm 2°$, similar to the pitch angles of other spiral arms.

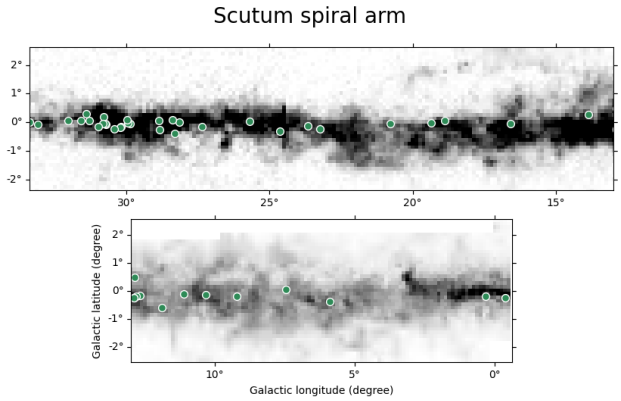

Figure 7. The Scutum spiral arm maser parallax sources (green dots) overplotted on the first quadrant CO data from [70,90] integrated within ± 15 km s^{-1} from the LSR velocities obtained by [9].

Sixteen high-mass star-forming regions in the Scutum arm exhibit large peculiar motions above 20 km s^{-1} of which 13 are oriented towards the Galactic Centre [93]. These large motions are measured in all three maser transitions used for parallax and proper motion measurements (6.7 and 12 GHz methanol masers, 22 GHz water masers). Although some sources in the Perseus spiral arm also show large peculiar motions, only in the Scutum arm such a large number of sources with large peculiar motions is found. This indicates that a local phenomenon affecting the sources in the Scutum spiral arm is the cause for these large peculiar motions. References [92,93] showed that the combined gravitational potential of the spiral arm and the Galactic bar could be a likely explanation.

6.6. Far Side of the Milky Way

The far side of the Milky Way beyond the Galactic Centre is still not well understood. Since distances to targets in this region are large, they require an even higher parallax accuracy than in the inner Galaxy. Foreground extinction from the dust in spiral arms makes the detection of star-forming regions at optical wavelengths difficult.

Within the Galactic longitude range $-10^\circ < l < 10^\circ$, the Galaxy rotates almost perpendicular to the Sun's line-of-sight. Using the kinematic distance method in this region is thus nearly impossible since the radial velocities are all close to zero.

With recent observations of the BeSSeL and VERA surveys progress has been made to pinpoint several high-mass star-forming regions on the far side of the Milky Way. Reference [47] observed 11 epochs with VERA towards 22 GHz water masers in the high-mass star-forming region G7.47+0.06. They measured a parallax of 0.170 ± 0.135 mas. Although it proved too difficult to determine an accurate parallax, the proper motion of the source was clearly detected. The proper motion along Galactic longitude is -5.03 ± 0.07 mas yr^{-1} and -0.01 ± 0.09 mas yr^{-1} along Galactic latitude [47]. Using the proper motion method of [46], the authors determined a distance of 20 ± 2 kpc to this source which locates it in the Scutum-Centaurus arm.

This source was also targeted with VLBA observations for six epochs. Reference [48] determined a parallax of 0.049 ± 0.006 mas for this source which corresponds to a distance of $20.4^{+2.8}_{-2.2}$ kpc, consistent with [47]. The position of G7.47+0.06 in the far segment of the Scutum arm is inconsistent with a spiral arm fit that assumes the same pitch angle of $\sim 20^\circ$ [92] as for the near segment of the arm. This indicates that a logarithmic spiral with a single pitch angle does not describe the Scutum spiral arm well [48].

Reference [73] reported parallax measurements of four 22 GHz water masers in distant star-forming regions. These sources were observed over 16 epochs with the VLBA. For G019.60−0.23 and G020.08−0.13 parallaxes of 0.076 ± 0.011 mas and 0.066 ± 0.010 mas, respectively, were measured, corresponding to distances of $13.2^{+2.2}_{-1.7}$ kpc and $15.2^{+2.7}_{-2.0}$ kpc, respectively. Since these two sources are located close on the sky and have similar line-of-sight velocities, the authors conclude that these sources are physically associated. They seem to be located in the Sagittarius arm but an association with the Perseus arm cannot be excluded due to their relatively large parallax error bars.

G020.77 − 0.05 and G026.50 + 0.28 have distances of $8.1^{+0.9}_{-0.8}$ kpc and $6.3^{+0.5}_{-0.4}$ kpc, respectively, which place them near the end of the Galactic bar. While [73] favour an association with the far side of the Scutum arm for the first source, they locate the second one in the Norma arm, the inner Galaxy extension of the Outer spiral arm.

7. Fundamental Galactic Parameters from Astrometry

Knowledge of the Galactic rotation curve, the Solar motion, and the distance from the Sun to the Galactic Centre are essential to understand the large-scale structure and kinematics of our Galaxy. These values determine the physical properties, such as the mass and the luminosity of our Galaxy, and the properties of the super-massive black hole at the Galactic Centre. Furthermore, precise distance measurements to the Galactic Centre are important for an accurate calibration of Cepheid period-luminosity relations, which can then be used to determine distances to other galaxies. Finally, the more precisely astronomers know the structure of the Milky Way galaxy, the better they can compare it with other galaxies and study spiral galaxies and star formation.

To measure these quantities accurately, precise 3D space and velocity information of objects across the Galactic disk are necessary. Currently, VLBI maser astrometry is one of the best methods to achieve these goals.

7.1. Using Maser Astrometry to Fit Galactic Parameters

The 3D motions of the high-mass star-forming regions (and a few red super giants) across the Galactic plane, obtained through VLBI maser astrometry, provide astronomers with pin points of velocity field information to which models of a Galactic rotation curve can be fitted. The motion of each of these high-mass star-forming regions will be a combination of the Galactic rotation at the Galactocentric distance of the star-forming region, its non-circular peculiar motion, and the Solar motion.

Both the BeSSeL and VERA surveys used a similar approach of the Bayesian Markov Chain Monte Carlo method, described in [41,96], where they fit a Galactic rotation curve

to the 3D motions of the high-mass star-forming regions. However, they used different parametrizations of the rotation curve, and different priors. They also fitted different maser astrometry data sets. Here, we discuss the latest results presented by these two surveys and the differences in their approaches.

The BeSSeL survey [9] tested four sets of priors, in which the initial guesses for the Solar motion and average peculiar motions of the maser stars in the plane (U_S and V_S) and their uncertainties were varied, and fitted the two-parameter universal rotation curve of [97] as the Galactic rotation curve. They used parallax and proper motion data of 147 high-mass star-forming regions, having removed sources with Galactocentric distances <4 kpc as these might possess large non-circular motions induced by the Galactic bar, sources with large (>20%) parallax uncertainties, and outlier sources with large peculiar motions (>3σ from mean) in any velocity component. The fitted parameters were the distance to the Galactic Centre (R_0), the 3D Solar motion, the mean peculiar motion of the high-mass star-forming regions in the Galactic plane ($\overline{U_S}$, $\overline{V_S}$), and two parameters that describe the universal rotation curve (the rotation curve fitting is discussed in Section 7.1.3). The statistical uncertainties were then derived by assuming a Gaussian probability distribution function (PDF). Their best fitting model was model A5 that uses loose priors for the Solar motion ($U_\odot = 11.1 \pm 1.2\,\mathrm{km\ s^{-1}}$, $V_\odot = 15 \pm 10\,\mathrm{km\ s^{-1}}$, $W_\odot = 7.2 \pm 1.1\,\mathrm{km\ s^{-1}}$) and for the average peculiar motions of the high-mass star-forming regions ($\overline{U_S} = 3 \pm 10\,\mathrm{km\ s^{-1}}$, $\overline{V_S} = -3 \pm 10\,\mathrm{km\ s^{-1}}$). The model A5 results for the distance to the Galactic Centre (R_0), the circular velocity at the Galactocentric distance of the Sun (Θ_0), and the angular rotation speed of the Sun $\Omega_\odot = (\Theta_0 + V_\odot)/R_0$ are quoted in Table 2 and discussed in more detail in the following Sections 7.1.1 and 7.1.2. The Galactic rotation curve results are discussed in Section 7.1.3.

The quantities $V_\odot$, $\overline{V_S}$ and Θ_0 are highly correlated (with Pearson coefficients of |0.74| and higher), and show the importance to accurately know the Solar motion to break the degeneracy. The model A5 values for the Solar motion are $U_\odot = 10.6 \pm 1.2$ km s^{-1}, $V_\odot = 10.7 \pm 6.0\,\mathrm{km\ s^{-1}}$ and $W_\odot = 7.6 \pm 0.7\,\mathrm{km\ s^{-1}}$, which are consistent with the values of [98] ($U_\odot = 11.1 \pm 1.2\,\mathrm{km\ s^{-1}}$, $V_\odot = 12.2 \pm 2.1\,\mathrm{km\ s^{-1}}$ and $W_\odot = 7.2 \pm 1.1\,\mathrm{km\ s^{-1}}$) with a larger uncertainty in $V_\odot$.

The parameters R_0 and Θ_0 are correlated with a Pearson coefficient of 0.45, similar to that found in [41]. This correlation has been investigated through simulations by [99] and found to depend mainly on the distribution of the high-mass star-forming regions in the Galactic plane and less so on their total number. This degeneracy can only be overcome by including new astrometry measurements of high-mass star-forming regions in the Southern Hemisphere.

Reference [9] found no significant lag for high-mass star-forming regions: $\overline{V_S} = -4.3 \pm 5.6\,\mathrm{km\ s^{-1}}$. However, significant inward motion towards the Galactic Centre has been found for star-forming regions: $\overline{U_S} = 6.0 \pm 1.4\,\mathrm{km\ s^{-1}}$, which is consistent with the [83] model of gas that is shocked when entering a spiral arm of low pitch angle.

The VERA survey [10] used a slightly larger set of 224 sources consisting of mostly high-mass star-forming regions and a few red super giants. Outliers with a peculiar motion $V_S > 50\,\mathrm{km\ s^{-1}}$ and with Galactocentric distances < 4 kpc were excluded from the model fitting due to their large non-circular motions that make these sources not representative of the Galactic rotation. Differently from [9,41], the VERA survey did not treat the Solar motion as a variable as it is highly correlated with the mean rotation of star-forming regions $\overline{V_S}$, but instead kept the Solar motion fixed to the values from [98]. Two types of rotation curves were fitted, a power-law and a second order polynomial. In their models, [10] fit for R_0, the Solar angular velocity $\Omega_\odot$, a 3D average peculiar velocity of the high-mass star-forming regions, and the rotation curve of choice. As for the BeSSeL survey, the statistical uncertainties quoted are based on assuming a Gaussian PDF distribution. However, the VERA survey also calculated the systematic uncertainties on R_0 and Ω_0 due to model and sample dependency (see Table 2). In both cases, the sample dependency resulted as the strongest source of systematic error.

The averaged peculiar motions of high-mass star-forming regions (averaging the results for the rotation curve parametrizations), $\overline{U_S}$ and $\overline{V_S}$, were both determined to be significant, and were oriented inwards towards the Galactic Centre ($\overline{U_S} = 4.3 \pm 1.0\,\mathrm{km\ s^{-1}}$) and with a slight lag in direction of Galactic rotation ($\overline{V_S} = -4.3 \pm 1.0\,\mathrm{km\ s^{-1}}$). The inward motion agrees with what is found by the BeSSeL survey. Also the value for the lag is consistent with the number found by the BeSSeL survey, but their uncertainties for this value are larger (rendering their measured value insignificant) because they also included the Solar motion in their fit.

Finally, it is also interesting to compare the fitting of fundamental Galactic parameters from maser stars with those of O-type stars with *Gaia* astrometry complemented with LSR velocities from [100]. Using the same approach as [41], Reference [66] analysed *Gaia* DR2 astrometry measurements of 291 O-type stars. They selected stars with parallax uncertainties better than 15% and peculiar motions smaller than 30 km s^{-1} (three times the stellar random motion). Fitting the O-star 3D motions, following the same approach as [41], for various types of rotation curves, they found that the universal rotation curve [97] gave the best results. The *Gaia*-based (DR2) results have larger uncertainties than the maser results but they are in good agreement (see Table 2). The larger error bars are due to worse astrometric accuracy of *Gaia* DR2 with respect to maser VLBI astrometry and lesser sampling of the spiral arm azimuth because the O-star *Gaia* astrometry has a limited reach in the Galactic midplane due to dust extinction.

Table 2. A summary of the measured values for the distance to the Galactic Centre R_0, the circular rotation speed at the Sun Θ_0, and the Solar angular rotation speed $\Omega_\odot$, where $\Omega_\odot = (\Theta_0 + V_\odot)/R_0$ [101–114].

Method	Result	Reference
	R_0—Distance to Galactic Centre (kpc)	
Maser astrometry	8.15 ± 0.15	[9]
Maser astrometry	$7.92 \pm 0.16_{\mathrm{stat}} \pm 0.3_{\mathrm{sys}}$	[10]
Maser and stellar astrometry	$8.15^{+0.04}_{-0.20}$	[101]
Stellar orbits	$8.275 \pm 0.009_{\mathrm{stat}} \pm 0.033_{\mathrm{sys}}$	[109]
Stellar orbits	$7.946 \pm 0.050_{\mathrm{stat}} \pm 0.032_{\mathrm{sys}}$	[108]
Kinematics of bar stars	8.23 ± 0.12	[103]
Stellar radial velocities	8.27 ± 0.29	[107]
Stellar astrometry	8.35 ± 0.18	[66]
Pop II Cepheids	$7.93 \pm 0.37_{\mathrm{stat}} \pm 0.26_{\mathrm{sys}}$	[106]
	Θ_0—circular rotation speed at the Sun (km s^{-1})	
Maser astrometry	236 ± 7	[9]
Maser astrometry	227 ± 5	[10]
Maser and stellar astrometry	236 ± 4.4	[101]
Stellar radial velocities	238 ± 9	[107]
Cepheid astrometry	233.6 ± 2.8	[110]
Cepheid astrometry	232.5 ± 0.83	[111]
Stellar astrometry	$229 \pm 0.2_{\mathrm{stat}}$	[112]
Stellar astrometry	240 ± 10	[66]
Stellar astrometry	240.7 ± 3.0	[113]
	$\Omega_\odot$—Full Solar angular rotation speed (km s^{-1} kpc^{-1})	
Maser astrometry	30.32 ± 0.27	[9]
Maser astrometry	$30.17 \pm 0.27_{\mathrm{stat}} \pm 0.3_{\mathrm{sys}}$	[10]
Sgr A* apparent motion	30.39 ± 0.04	[114]
Maser and stellar astrometry	30.51 ± 0.34	[101]
Stellar astrometry	30.57 ± 0.43	[66]

7.1.1. Distance to the Galactic Centre

The two distances to the Galactic Centre obtained through VLBI maser parallaxes, 8.15 ± 0.15 kpc [9] and $7.92 \pm 0.16_{\mathrm{stat}} \pm 0.3_{\mathrm{sys}}$ kpc [10], are in good agreement. A further analysis by [101] combined maser VLBI astrometry [9,10,77,102] with stellar continuum VLBI astrometry from the GOBELINS programme [5,7,8] and obtained a distance to the Galactic Centre of $8.15^{+0.04}_{-0.20}$ kpc, in full agreement with the maser astrometry results.

The VLBI maser astrometry results are also in agreement with Galactic Centre distances obtained through various other methods as summarized in Table 2. Reference [103] found 8.23 ± 0.12 kpc through the combination of *Gaia* EDR3 [3] and Apache Point Observatory galactic evolution experiment (APOGEE) DR17 [104] astrometry of Galactic bar stars

augmented spectro-photometric distances from the neural network method `astroNN`. *Gaia* DR2 [57] astrometry of O-type stars yielded 8.35 ± 0.18 kpc [105]. Using Pop II Cepheids, [106] found $7.93 \pm 0.37_{\rm stat} \pm 0.26_{\rm sys}$ kpc. By modelling the Galactic rotation with stellar radial velocities [107] determined 8.27 ± 0.29 kpc. The most precise measures of the distance to the Galactic Centre to date are from infrared astrometry, in particular from the analysis of the dynamics of stellar orbits around the black hole in the inner 10 arcseconds of the Galactic Centre. These measurements and analysis have yielded distances of $7.946 \pm 0.050_{\rm stat} \pm 0.032_{\rm sys}$ kpc obtained with Adaptive Optics with the Keck telescope [108], and $8.275 \pm 0.009_{\rm stat} \pm 0.033_{\rm sys}$ kpc obtained with the Very Large Telescope Interferometer (VLTI) [109]. While the two distances derived from stellar orbits are in slight tension with each other, the maser-parallax derived distances, which have larger uncertainties, are in agreement with both these values.

7.1.2. Solar Rotation Speed

The Solar angular rotation speed, $\Omega_\odot = (\Theta_0 + V_\odot)/R_0$, depends on the Galactic circular rotation speed at the Sun's position, Θ_0, on the Solar proper motion in the direction of Galactic rotation, $V_\odot$, and the distance to the Galactic Centre R_0. Table 2 summarizes the various measured results of Θ_0 and $\Omega_\odot$ obtained from VLBI maser astrometry and other methods.

The VLBI maser parallax results from BeSSeL and VERA for the circular rotation speed at the Sun's position are in agreement within their joint uncertainties: 236 ± 7 km s^{-1} [9] and 227 ± 5 km s^{-1} [10]. Also the result obtained from maser astrometry and radio star astrometry (using, among others, BeSSeL and VERA data, see Section 7.1.1 for a data provenance list), 236.4 ± 3.3 km s^{-1} [101], is consistent. The circular rotation speed at the position of the Sun obtained from *Gaia* DR2 [57] astrometry combined with distances derived from infrared period-luminosity relations [115] of Classical Cepheids, 233.6 ± 2.8 km s^{-1}[110] is in excellent agreement with the maser astrometry results. Also the values obtained from *Gaia* DR2 astrometry of O-type stars, 240 ± 10 km s^{-1} [66], and from stellar radial velocities, 238 ± 9 km s^{-1} [107], agree well with the maser astrometry results. *Gaia* EDR3 data of OB stars find 240.7 ± 3.0 km s^{-1} [113], notably close to the *Gaia* O-star result [66]. The Solar rotation speeds from maser parallaxes also agree with the Classical Cepheid result of [111], 232.5 ± 0.83 km s^{-1}, based on Cepheid data from a wide range of surveys. The value obtained through red giant branch (RGB) star astrometry and spectroscopy by [112] of $229 \pm 0.2_{\rm stat}$ km s^{-1} is at the lower limit of the BeSSeL value, and closer to the VERA value.

As mentioned before, the circular velocity at the Sun's position in the Galactic plane is strongly correlated with $V_\odot$, and the sum of the two, the full circular rotation speed $\Theta_0 + V_\odot$, can be constrained more accurately. The maser astrometry results for $\Theta_0 + V_\odot$ are 247 ± 4 km s^{-1} [9] and 239 ± 5 km s^{-1} [10], respectively. These numbers can be directly compared with the very precise measure of the apparent proper motion of Sgr A* in Galactic longitude of -6.411 ± 0.008 mas yr^{-1} from [114]. Under the assumption that the supermassive black hole Sgr A* is stationary, the apparent motion of Sgr A* can be interpreted as the reflex motion of the Solar motion in the direction of Galactic rotation. Using the distance to the Galactic Centre one can then transform the apparent proper motion of Sgr A* to the full Solar velocity in the direction of Galactic rotation. The Sgr A* proper motion result of [114] combined with the distance of 8.15 kpc [9] shows that the Sun is moving by 247.69 ± 0.33 km s^{-1} in the direction of Galactic rotation (note the sign inversion). The BeSSeL result is in excellent agreement with this value, while the VERA result is a bit smaller.

When dividing $\Theta_0 + V_\odot$ by the distance to the Galactic Centre, one can determine $\Omega_\odot$, the full Solar angular velocity. The maser astrometry results yield 30.32 ± 0.27 km s^{-1} kpc^{-1} [9] and $30.17 \pm 0.27_{\rm stat} \pm 0.3_{\rm sys}$ km s^{-1} kpc^{-1} [10], respectively. The best constrain for this value is the apparent motion measure of Sgr A* in Galactic longitude which yields 30.39 ± 0.04 km s^{-1} kpc^{-1} [114]. This result is in excellent agreement with the BeSSeL value, and well within the uncertainty of the VERA result.

The determination of the fundamental Galactic parameters R_0 and Ω_0 using the 3D velocity data of maser-emitting star-forming regions across the Galaxy [9,10], and the agreement of these results with the distance measure from stellar orbits around Sgr A* in the infrared [108,109] and the measured apparent proper motion of Sgr A* [114] are strong evidence that Sgr A* is at the dynamical centre of the Milky Way.

7.1.3. Galactic Rotation Curve

Maser-bearing high-mass star-forming regions can be used to fit the Galactic rotation curve. Figure 8 shows the maser astrometry data for the V motion (motion in the direction of Galactic rotation) versus Galactocentric radius from 4 kpc outwards. Up to 10 kpc, the targets cover the range of Galactocentric radii well, but beyond that the distribution of star-forming regions with maser astrometry is more sparse.

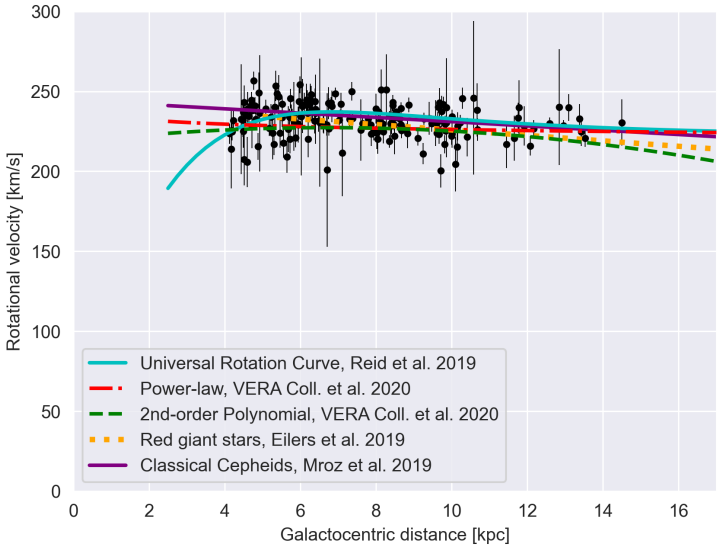

Figure 8. Galaxy rotation curves derived from maser VLBI astrometry surveys (BeSSeL [9], VERA [10]), from red giant stars ([112]) and from Classical Cepheids ([110]). The rotational velocities and Galactocentric distances of maser-bearing high-mass star-forming regions taken from the BeSSeL and VERA surveys are shown as black dots. Sources with Galactocentric distances <4 kpc, sources with >30% parallax uncertainties, sources with >50 km s^{-1} motion in direction of Galactic rotation, and outlier sources (see [9]) are not plotted.

Rotation curves fitted to maser stars use objects with Galactocentric distances of 4 kpc and larger as the motion of maser stars in the inner part of the disk is expected to be heavily influenced by the Galactic bar.

The BeSSeL survey [9] fitted the universal rotation curve of [97] to the maser data. The rotation curve is composed of a disk and a halo velocity component. Following the Note added in Proof in [97], the universal rotation curve can be fitted with only two parameters, $a2 = R_{\rm opt}/R_0$, where $R_{\rm opt}$ is the Galactocentric radius encircling 83% of the total integrated light, and $a3 = 1.5(L/L^\star)^{0.2}$, where L is the galaxy luminosity relative to a $L^\star$ galaxy with $L^\star = 10^{10.4} L_\odot$. The rotational velocity at R_0 can be obtained by scaling relations of $R_{\rm opt}$, velocity, and luminosity. The BeSSeL A5 fit gives $a2 = 0.96 \pm 0.05$ and $a3 = 1.62 \pm 0.02$.

The VERA survey [10] performed two rotation curve fits, one with a power law and one with a second order polynomial. The power law fit of the Galactic rotation is:

$$\Theta(R) = \Theta_0 (R/R_0)^\alpha, \tag{3}$$

where $R_0 = 7.92 \pm 0.16$ kpc, $\Theta_0 = 227 \pm 5$ km s^{-1}, and $\alpha = -0.016 \pm 0.012$ [10]. The second order polynomial equation for the Galactic rotation is:

$$\Theta(R) = \Theta_0 + a_0(R - R_0) + b_0(R - R_0)^2, \quad (4)$$

where $R_0 = 7.97 \pm 0.15$ kpc, $\Theta_0 = 228 \pm 5$ km s^{-1}, and $a_0 = -0.5 \pm 0.4$ km s^{-1} kpc^{-1} and $b = -0.2 \pm 0.1$ km s^{-1} kpc^{-1} [10].

The maser astrometry rotation curves can be compared with rotation curves derived based on other types of objects, such as Classical Cepheids or RGB stars. For these evolved stars, there are more objects available at farther Galactocentric radii: up to ∼18 kpc for Cepheids and up to ∼20 kpc for RGB stars (beyond that the uncertainties on the velocity grow rapidly).

The RGB star rotation curve was determined by [112]. These authors used spectro-photometric parallaxes of AGB stars, from a combination of *APOGEE* DR14 spectroscopy [115,116] with *Gaia* DR2 [57], *2MASS* [117], and *WISE* photometry [118], and find a smooth rotation curve between Galactocentric distances $5 \lesssim R \lesssim 25$ kpc, well described by a linear function:

$$\Theta(R) = (229 \pm 0.02)\,\mathrm{km\,s^{-1}} - (1.7 \pm 0.1)\,\mathrm{km\,s^{-1}\,kpc^{-1}} \times (R - R_0). \quad (5)$$

Another interesting comparison is the rotation curve derived by [110] using 773 Classical Cepheids. Their best model, a linear function, is given by:

$$\Theta(R) = (233.6 \pm 2.02)\,\mathrm{km\,s^{-1}} - (1.34 \pm 0.2)\,\mathrm{km\,s^{-1}\,kpc^{-1}} \times (R - R_0). \quad (6)$$

Figure 8 shows the three rotation curves based on maser parallaxes and the two rotation curves based on RGB stars and Classical Cepheid stars. Between 5 and 12 kpc, the rotation curves have a similar slope; they are nearly flat. The two evolved star rotation curves are in good agreement with the maser data points.

Looking at the rotation curves in more detail, however, one can note that the universal rotation curve by [9] has a slightly different shape than the linear curves, and that it has, on average, higher rotational velocities in this Galactocentric distance range. Beyond 10–12 kpc, the rotation curves start to diverge more: while the universal rotation curve of [9], the power-law fit of [10] and the Cepheid-based linear rotation curve of [110] are around 224 km s^{-1} and remain flat at these large Galactocentric distances, the second order polynomial fit of [10] and the RSG-based linear rotation curve of [112] decrease with distance from the Galactic Centre. The maser data agree well with the rotation curves that are close to flat at distances of 12–15 kpc. However, more maser stars with precise astrometry, and, in particular, maser stars at large Galactocentric distances, are needed to better constrain the type and thus the shape of the Galactic rotation curve. Finding high-mass star-forming regions with maser emission at large Galactocentric distances is not simple: the star-forming activity in the Outer arm is rather low and decreases further at distances beyond the Outer arm.

7.2. The Galactic Plane

High-mass star-forming regions are expected to be located very close to the Galactic plane and therefore may be used to refine the IAU-defined Galactic plane. Reference [119] in their Figure 5 showed how methanol masers trace the Galactic plane better than HII regions or giant molecular clouds. The distance perpendicular to the Galactic plane (Z) can be obtained from the 3D position (X, Y, Z) calculated from the parallax-based distance and Galactic coordinates (l, b).

Reference [9] examined the Z-distribution of high-mass star-forming regions within 7 kpc of the Galactic Centre, to avoid effects of disk warping. Indeed, these star-forming regions have a tight distribution in the IAU-defined Galactic plane with, however, more sources at negative Z_{IAU}, thus indicating that the Sun is located above the Galactic plane. Based on this sample of high-mass star-forming regions, [9] derived the Sun's height above the Galactic plane to be $Z_\odot = 5.5 \pm 5.8$ pc.

Shifting Sgr A* by 5.5 pc brings it from its apparent Galactic latitude of $b = -0.046°$ closer to the Galactic plane ($b = -0.007°$) where one would dynamically expect it to be.

The result of [9] is in agreement with values for the Sun's height above the Galactic plane of 5.7 ± 0.5 pc and 7.6 ± 0.4 pc, derived from methanol masers and HII regions, respectively, which are located in the inner Galaxy (Galactocentric distances $< R_0$), excluding the Local arm masers [119]. Also the results of [120], based on HII regions in the first Galactic quadrant and the inner Galaxy, yield results between 3 and 6 pc for different rotation curves and spatial sub-selections. Interestingly, literature values of $Z_\odot$ vary between 5 and 40 pc (see [9] and references therein). Potential origins for this variation can be the extinction in the Galactic plane and Galactic warping [9] and the Local arm which was found to affect the Z distribution pattern [119].

7.3. Structure in the Galactic Z-Height

Using the previous determined shift in Z-position, the maser stars can be shifted to their true Z-positions. Doing this, [9] then find that high-mass star-forming regions have a scale height of 19 ± 2 pc – tracing the Galactic plane very accurately for sources within 7 kpc Galactocentric distance.

Figure 9 shows the Z-height of the high-mass star-forming regions, for which BeSSeL and VERA measurements are available, in seven 30-degree azimuth ranges. Beyond 7 kpc, the Z-height of high-mass star-forming regions is increasingly scattered, partially due to the expected Galactic warp and partially due to intrinsic scatter of the sources. Notably in the $30° < \beta < 60°$ azimuth range a clear trend of increase in Z-height with Galactocentric distance is seen.

Reference [77] explored these sources with $d > 7$ kpc. In the Galactic azimuth range of $20° < \beta < 50°$ they fitted a sinusoidal curve to the Z-height distribution and W motion of the star-forming regions. Their results yield that the Galactic warp reaches out to 200−600 pc toward the north Galactic pole. The W motion, positive towards the north Galactic pole, of these targets could also be well fitted with a sinusoidal curve, with an amplitude of about 10 km s^{-1} reaching 0 km s^{-1} at the maximum of the Z-height amplitude. The wave-like distribution is also seen in the classical Cepheid population ([115] in their Figure 2B, box $315° < \phi < 330°$).[5] Classical Cepheids are supergiant stars with ages < 400 Myr and especially the youngest classical Cepheids are considered good tracers of the Galactic disk (see also [120,121]). As to the origin of this wave-like structure, Ref. [77] suggest that this can be explained well with a perturbation by the Sagittarius dwarf galaxy when passing through the Milky Way as described in [122].

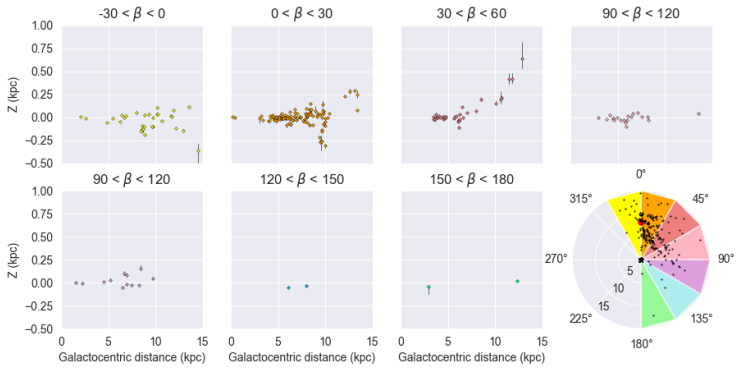

Figure 9. The Z-location of high-mass star-forming regions with maser astrometry data taken from [9,10,73] versus Galactocentric distance shown in seven 30-degree azimuth ranges. The bottom right plot shows a plan view of the Milky Way with the azimuth ranges indicated by colors. The Sun is denoted as a red dot, and the Galactic Centre (located at (0,0)) by a black star symbol.

8. Summary and Outlook

Over the last decade, VLBI maser astrometry has allowed astronomers to trace the structure of our Galaxy. The parallax and proper motion measurements of more than 200 maser stars pinpoint several major spiral arms, in particular in the first and second Galactic quadrants (Figure 10). The VLBI results have permitted astronomers to determine the distance to the Galactic Centre and fit a Galactic rotation curve, determining also the Solar angular and rotational velocities. These results are in agreement with the latest stellar astrometry results from VLTI and Keck, and with *Gaia* and Cepheid based results.

In the third quadrant, the Outer and Perseus spiral arms are dying out past longitude of 240°. Due to the lack of star-forming regions the number of parallax measurements is sparse. The fourth quadrant is only observable from the Southern hemisphere. The locations of the spiral arms in this part of the Galaxy are less accurate since they are inferred mostly from the spiral arm models fitted to the data in quadrants 1 and 2. However, the tangent points of each arm in quadrant 4 are used to constrain the arm extrapolations.

Figure 10. Artistic impression of the Milky Way based on 200 trigonometric parallaxes of maser sources, presenting our Galaxy as a barred spiral galaxy with four major spiral arms and additional arm segments and spurs (Credit: Xing-Wu Zheng & Mark Reid; BeSSeL/NJU/CFA).

Ongoing and future maser astrometry projects with VLBI arrays in the Southern Hemisphere, in particular with the Square Kilometre Array (SKA), will ameliorate this situation and deliver a complete picture of the spiral arm structure of the Milky Way. Reference [123] summarizes the upcoming opportunities for maser astrometry when including the SKA in existing VLBI arrays.

Improvements of the astrometric accuracy, especially for methanol maser observations, will further allow a better coverage of the full Galactic plane. A review of the technical improvements including the multi-view technique is discussed in [124].

The AuScope (Australia Telescope) project which uses a dedicated VLBI array of four antennas in Australia (Ceduna 30-m, Yarragadee 12-m, Katherine-12 m, Hobart 12-m) and one in New Zealand (Warkworth 30-m) is now in its second year of parallax observations and is planned to run for five years. Each year about ten 6.7 GHz methanol masers are targeted with eight tracks each. The "inverse MultiView" calibration technique [125] which allows for a parallax accuracy of 6.7 GHz methanol masers of 10 μas was specifically developed for this project.

Author Contributions: Conceptualization, K.I. and K.L.J.R.; data curation, K.L.J.R.; investigation, K.I. and K.L.J.R.; project administration, K.I.; visualization, K.I. and K.L.J.R.; writing—original draft preparation, K.I. and K.L.J.R.; writing—review and editing, K.I. and K.L.J.R. All authors have read and agreed to the published version of the manuscript.

Funding: This research received no external funding.

Acknowledgments: The authors are grateful to Mareki Honma and Mark Reid for providing valuable comments on a first draft of the manuscript.

Conflicts of Interest: The authors declare no conflict of interest.

Notes

1 The BeSSeL website is available at http://bessel.vlbi-astrometry.org/ (accessed on 18 July 2022).

2 The VERA website is available at https://www.miz.nao.ac.jp/veraserver/ (accessed on 18 July 2022).

3 The *Gaia* archive is available at https://gea.esac.esa.int/archive/ (accessed on 18 July 2022).

4 The updated version of the parallax-based distance calculator can be found here http://bessel.vlbi-astrometry.org/node/378 (accessed on 18 July 2022).

5 Their azimuth ϕ is defined counter clockwise, starting at the Solar azimuth, while in this review, azimuth β is defined as increasing clockwise.

References

1. Hubble, E.P. Extragalactic nebulae. *Astrophys. J.* **1926**, *64*, 321–369. [CrossRef]
2. de Vaucouleurs, G. *Statistics of Spiral Patterns and Comparison of Our Galaxy with Other Galaxies*; The Spiral Structure of our Galaxy; Becker, W., Kontopoulos, G.I., Eds.; Reidel: Dordrecht, The Netherlands, 1970; Volume 38, p. 18.
3. Brown, A.G.A. et al. [Gaia Collaboration]. Gaia Early Data Release 3. Summary of the contents and survey properties. *Astrophys. Galaxies* **2021**, *649*, A1. [CrossRef]
4. Ortiz-León, G.N.; Loinard, L.; Kounkel, M.A.; Dzib, S.A.; Mioduszewski, A.J.; Rodríguez, L.F.; Torres, R.M.; González-López lira, R.A.; Pech, G.; Rivera, J.L.; et al. The Gould's Belt Distances Survey (GOBELINS). I. Trigonometric Parallax Distances and Depth of the Ophiuchus Complex. *Astrophys. J.* **2017**, *834*, 141. [CrossRef]
5. Kounkel, M.; Hartmann, L.; Loinard, L.; Ortiz-León, G.N.; Mioduszewski, A.J.; Rodríguez, L.F.; Dzib, S.A.; Torres, R.M.; Pech, G.; Galli, P.A.B.; et al. The Gould's Belt Distances Survey (GOBELINS) II. Distances and Structure toward the Orion Molecular Clouds. *Astrophys. J.* **2017**, *834*, 142. [CrossRef]
6. Ortiz-León, G.N.; Dzib, S.A.; Kounkel, M.A.; Loinard, L.; Mioduszewski, A.J.; Rodríguez, L.F.; Torres, R.M.; Pech, G.; Rivera, J.L.; Hartmann, L.; et al. The Gould's Belt Distances Survey (GOBELINS). III. The Distance to the Serpens/Aquila Molecular Complex. *Astrophys. J.* **2017**, *834*, 143. [CrossRef]
7. Galli, P.A.B.; Loinard, L.; Ortiz-Léon, G.N.; Kounkel, M.; Dzib, S.A.; Mioduszewski, A.J.; Rodríguez, L.F.; Hartmann, L.; Teixeira, R.; Torres, R.M.; et al. The Gould's Belt Distances Survey (GOBELINS). IV. Distance, Depth, and Kinematics of the Taurus Star-forming Region. *Astrophys. J.* **2018**, *859*, 33. [CrossRef]
8. Ortiz-León, G.N.; Loinard, L.; Dzib, S.A.; Galli, P.A.B.; Kounkel, M.; Mioduszewski, A.J.; Rodríguez, L.F.; Torres, R.M.; Hartmann, L.; Boden, A.F.; et al. The Gould's Belt Distances Survey (GOBELINS). V. Distances and Kinematics of the Perseus Molecular Cloud. *Astrophys. J.* **2018**, *865*, 73. [CrossRef]
9. Reid, M.J.; Menten, K.M.; Brunthaler, A.; Zheng, X.W.; Dame, T.M.; Xu, Y.; Li, J.; Sakai, N.; Wu, Y.; Immer, K.; et al. Trigonometric Parallaxes of High-mass Star-forming Regions: Our View of the Milky Way. *Astrophys. J.* **2019**, *885*, 131. [CrossRef]
10. Hirota, T. et al. [VERA Collaboration]. The First VERA Astrometry Catalog. *Publ. Astron. Soc. Jpn.* **2020**, *72*, 50. [CrossRef]
11. Goddi, C.; Moscadelli, L.; Sanna, A. Infall and outflow within 400 AU from a high-mass protostar. 3D velocity fields from methanol and water masers in AFLG 5142. *Astrophys. Galaxies* **2011**, *535*, L8. [CrossRef]
12. Sanna, A.; Reid, M.J.; Carrasco-González, C.; Menten, K.M.; Brunthaler, A.; Moscadelli, L.; Rygl, K.L.J. Clustered Star Formation and Outflows in AFGL 2591. *Astrophys. J.* **2012**, *745*, 191. [CrossRef]
13. Moscadelli, L.; Xu, Y.; Chen, X. Revising the Kinematics of 12 GHz CH_3OH Masers Toward W3(OH). *Astrophys. J.* **2010**, *716*, 1356–1370. [CrossRef]
14. Sanna, A.; Moscadelli, L.; Surcis, G.; van Langevelde, H.J.; Torstensson, K.J.E.; Sobolev, A.M. Planar infall of CH_3OH gas around Cepheus A HW2. *Astrophys. Galaxies* **2017**, *603*, A94. [CrossRef]
15. Brunthaler, A.; Reid, M.J.; Menten, K.M.; Zheng, X.W.; Bartkiewicz, A.; Choi, Y.K.; Dame, T.; Hachisuka, K.; Immer, K.; Moellenbrock, G.; et al. The Bar and Spiral Structure Legacy (BeSSeL) survey: Mapping the Milky Way with VLBI astrometry. *Astron. Nachrichten* **2011**, *332*, 461. [CrossRef]
16. Immer, K.; Brunthaler, A.; Reid, M.J.; Bartkiewicz, A.; Choi, Y.K.; Menten, K.M.; Moscadelli, L.; Sanna, A.; Wu, Y.W.; Xu, Y.; et al. The VLBA Calibrator Search for the BeSSeL Survey. *Astrophys. J. Suppl.* **2011**, *194*, 25. [CrossRef]

17. Reid, M.J.; Menten, K.M.; Brunthaler, A.; Zheng, X.W.; Moscadelli, L.; Xu, Y. Trigonometric Parallaxes of Massive Star-Forming Regions. I. S 252 & G232.6+1.0. *Astrophys. J.* **2009**, *693*, 397–405. [CrossRef]
18. Reid, M.J.; Brunthaler, A. The Proper Motion of Sagittarius A*. II. The Mass of Sagittarius A*. *Astrophys. J.* **2004**, *616*, 872–884. [CrossRef]
19. Walker, C.; Chatterjee, S. VLBA Scientific Memo 23. Available online: https://library.nrao.edu/public/memos/vlba/sci/VLBAS_23.pdf (accessed on 8 May 2022).
20. Reid, M.J.; Brunthaler, A.; Menten, K.M.; Sanna, A.; Xu, Y.; Li, J.J.; Wu, Y.; Hu, B.; Zheng, X.W.; Zhang, B.; et al. Techniques for Accurate Parallax Measurements for 6.7 GHz Methanol Masers. *Astron. J.* **2017**, *154*, 63. [CrossRef]
21. Wu, Y.W.; Reid, M.J.; Sakai, N.; Dame, T.M.; Menten, K.M.; Brunthaler, A.; Xu, Y.; Li, J.J.; Ho, B.; Zhang, B.; et al. Trigonometric Parallaxes of Star-forming Regions beyond the Tangent Point of the Sagittarius Spiral Arm. *Astrophys. J.* **2019**, *874*, 94. [CrossRef]
22. Greisen, E.W. AIPS, the VLA, and the VLBA. In *Information Handling in Astronomy—Historical Vistas*; Heck, A., Ed.; Astrophysics and Space Science Library; Kluwer Academic Publishers: Dordrecht, The Netherlands, 2003; Volume 285, pp. 109–125. [CrossRef]
23. Kettenis, M.; Sipior, M. *ParselTongue: AIPS Python Interface*; record ascl:1208.020; Astrophysics Source Code Library: Dordrecht, The Netherlands, 2012.
24. Honma, M.; Kijima, M.; Suda, H.; Kawaguchi, N.; Kobayashi, H.; Bushimata, T.; Shimizu, R.; Yoshimura, A.; Sasao, T.; Hirota, T.; et al. Dual-Beam Delay Calibration for VERA. *Publ. Astron. Soc. Jpn.* **2008**, *60*, 935–950. [CrossRef]
25. Beasley, A.J.; Gordon, D.; Peck, A.B.; Petrov, L.; MacMillan, D.S.; Fomalont, E.B.; Ma, C. The VLBA Calibrator Survey-VCS1. *Astrophys. J. Suppl.* **2002**, *141*, 13–21. [CrossRef]
26. Petrov, L.; Hirota, T.; Honma, M.; Shibata, K.M.; Jike, T.; Kobayashi, H. VERA 22 GHz Fringe Search Survey. *Astron. J.* **2007**, *133*, 2487–2494. [CrossRef]
27. Petrov, L.; Honma, M.; Shibata, S.M. The KCAL VERA 22 GHz Calibrator Survey. *Astron. J.* **2012**, *143*, 35. [CrossRef]
28. Ulich, B.L.; Haas, R.W. Absolute calibration of millimeter-wavelength spectral lines. *Astrophys. J. Suppl.* **1976**, *30*, 247–258. [CrossRef]
29. Honma, M.; Tamura, Y.; Reid, M.J. Tropospheric Delay Calibrations for VERA. *Publ. Astron. Soc. Jpn.* **2008**, *60*, 951. [CrossRef]
30. Nagayama, T.; Hirota, T.; Honma, M.; Kurayama, T.; Adachi, Y.; Tamura, Y.; Kanya, Y. VEDA: VERA data analysis software for VLBI phase-referencing astrometry. *Publ. Astron. Soc. Jpn.* **2020**, *72*, 51. [CrossRef]
31. Rygl, K.L.J.; Brunthaler, A.; Reid, M.J.; Menten, K.M.; van Langevelde, H.J.; Xu, Y. Trigonometric parallaxes of 6.7 GHz methanol masers. *Astrophys. Galaxies* **2010**, *511*, A2. [CrossRef]
32. Rygl, K.L.J.; Brunthaler, A.; Sanna, A.; Menten, K.M.; Reid, M.J.; van Langevelde, H.J.; Honma, M.; Torstensson, K.J.E.; Fujisawa, K. Parallaxes and proper motions of interstellar masers toward the Cygnus X star-forming complex. I. Membership of the Cygnus X region. *Astrophys. Galaxies* **2012**, *539*, A79. [CrossRef]
33. Menten, K.M. The Discovery of a New, Very Strong, and Widespread Interstellar Methanol Maser Line. *Astrophys. J. Lett.* **1991**, *380*, L75. [CrossRef]
34. Brunthaler, A.; Reid, M.J.; Falcke, H. Atmosphere-Corrected Phase-Referencing. In *Future Directions in High Resolution Astronomy*; Romney, J., Reid, M., Eds.; Astronomical Society of the Pacific: San Francisco, CA, USA, 2005; Volume 340, p. 455.
35. Fomalont, E.B.; Petrov, L.; MacMillan, D.S.; Gordon, D.; Ma, C. The Second VLBA Calibrator Survey: VCS2. *Astron. J.* **2003**, *126*, 2562–2566. [CrossRef]
36. Petrov, L.; Kovalev, Y.Y.; Fomalont, E.; Gordon, D. The Third VLBA Calibrator Survey: VCS3. *Astron. J.* **2005**, *129*, 1163–1170. [CrossRef]
37. Petrov, L.; Kovalev, Y.Y.; Fomalont, E.B.; Gordon, D. The Fourth VLBA Calibrator Survey: VCS4. *Astron. J.* **2006**, *131*, 1872–1879. [CrossRef]
38. Kovalev, Y.Y.; Petrov, L.; Fomalont, E.B.; Gordon, D. The Fifth VLBA Calibrator Survey: VCS5. *Astron. J.* **2007**, *133*, 1236–1242. [CrossRef]
39. Ma, C.; Arias, E.F.; Eubanks, T.M.; Fey, A.L.; Gontier, A.M.; Jacobs, C.S.; Sovers, O.J.; Archinal, B.A.; Charlot, P. The International Celestial Reference Frame as Realized by Very Long Baseline Interferometry. *Astron. J.* **1998**, *116*, 516–546. [CrossRef]
40. Condon, J.J.; Cotton, W.D.; Greisen, E.W.; Yin, Q.F.; Perley, R.A.; Taylor, G.B.; Broderick, J.J. The NRAO VLA Sky Survey. *Astron. J.* **1998**, *115*, 1693–1716. [CrossRef]
41. Reid, M.J.; Menten, K.M.; Brunthaler, A.; Zheng, X.W.; Dame, T.M.; Xu, Y.; Wu, Y.; Zhang, B.; Sanna, A.; Sato, M.; et al. Trigonometric Parallaxes of High Mass Star Forming Regions: The Structure and Kinematics of the Milky Way. *Astrophys. J.* **2014**, *783*, 130. [CrossRef]
42. Krishnan, V.; Ellingsen, S.P.; Reid, M.J.; Brunthaler, A.; Sanna, A.; McCallum, J.; Reynolds, C.; Bignall, H.E.; Phillips, C.J.; Dodson, R.; et al. First Parallax Measurements Towards a 6.7 GHz Methanol Maser with the Australian Long Baseline Array—Distance to G 339.884-1.259. *Astrophys. J.* **2015**, *805*, 129. [CrossRef]
43. Zhang, B.; Reid, M.J.; Menten, K.M.; Zheng, X.W.; Brunthaler, A.; Dame, T.M.; Xu, Y. Parallaxes for W49N and G048.60+0.02: Distant Star Forming Regions in the Perseus Spiral Arm. *Astrophys. J.* **2013**, *775*, 79. [CrossRef]
44. Rioja, M.J.; Dodson, R.; Orosz, G.; Imai, H.; Frey, S. MultiView High Precision VLBI Astrometry at Low Frequencies. *Astron. J.* **2017**, *153*, 105. [CrossRef]
45. Nagayama, T.; Omodaka, T.; Handa, T.; Honma, M.; Kobayashi, H.; Kawaguchi, N.; Ueno, Y. Astrometry of Galactic Star-Forming Region G48.61+0.02 with VERA. *Publ. Astron. Soc. Jpn.* **2011**, *63*, 719–725. [CrossRef]

46. Sofue, Y. Accuracy Diagrams for the Galactic Rotation Curve and Kinematical Distances. *Publ. Astron. Soc. Jpn.* **2011**, *63*, 813. [CrossRef]
47. Yamauchi, A.; Yamashita, K.; Honma, M.; Sunada, K.; Nakagawa, A.; Ueno, Y. The far distance to G7.47+0.06 from proper motion measurement of H_2O masers. *Publ. Astron. Soc. Jpn.* **2016**, *68*, 60. [CrossRef]
48. Sanna, A.; Reid, M.J.; Dame, T.M.; Menten, K.M.; Brunthaler, A. Mapping spiral structure on the far side of the Milky Way. *Science* **2017**, *358*, 227–230. [CrossRef] [PubMed]
49. Schultz, G.V.; Sherwood, W.A.; Winnberg, A. Radial diameters of Type II OH/IR sources. *Astrophys. Galaxies* **1978**, *63*, L5–L7.
50. van Langevelde, H.J.; van der Heiden, R.; van Schooneveld, C. Phase lags from multiple flux curves of OH/IR stars. *Astrophys. Galaxies* **1990**, *239*, 193–204.
51. Etoka, S.; Engels, D.; Gérard, E.; Richards, A.M.S. Distances of Stars by mean of the Phase-lag Method. In *Astrophysical Masers: Unlocking the Mysteries of the Universe*; Tarchi, A., Reid, M.J., Castangia, P., Eds.; Cambridge University Press (CUP): Cambridge, UK, 2018; Volume 336, pp. 381–384. [CrossRef]
52. Orosz, G.; Imai, H.; Dodson, R.; Rioja, M.J.; Frey, S.; Burns, R.A.; Etoka, S.; Nakagawa, A.; Nakanishi, H.; Asaki, Y.; et al. Astrometry of OH/IR Stars Using 1612 MHz Hydroxyl Masers. I. Annual Parallaxes of WX Psc and OH138.0+7.2. *Astron. J.* **2017**, *153*, 119. [CrossRef]
53. Whitelock, P.; Feast, M.; Catchpole, R. IRAS sources and the nature of the Galactic Bulge. *Mon. Not. RAS* **1991**, *248*, 276. [CrossRef]
54. Reid, M.J.; Menten, K.M.; Zheng, X.W.; Brunthaler, A.; Moscadelli, L.; Xu, Y.; Zhang, B.; Sato, M.; Honma, M.; Hirota, T.; et al. Trigonometric Parallaxes of Massive Star-Forming Regions. VI. Galactic Structure, Fundamental Parameters, and Noncircular Motions. *Astrophys. J.* **2009**, *700*, 137–148. [CrossRef]
55. Vallenari, A. et al. [Gaia Collaboration]. Gaia Data Release 3: Summary of the contents and survey properties. *Astrophys. Galaxies* 2022, *Forthcoming article*.
56. Xu, S.; Zhang, B.; Reid, M.J.; Zheng, X.; Wang, G. Comparison of Gaia DR2 Parallaxes of Stars with VLBI Astrometry. *Astrophys. J.* **2019**, *875*, 114. [CrossRef]
57. Brown, A.G.A. et al. [Gaia Collaboration]. Gaia Data Release 2. Summary of the contents and survey properties. *Astrophys. Galaxies* **2018**, *616*, A1. [CrossRef]
58. Sudou, H.; Omodaka, T.; Murakami, K.; Nagayama, T.; Nakagawa, A.; Urago, R.; Nagayama, T.; Hirano, K.; Honma, M. Annual parallax measurements of a semi-regular variable star SV Pegasus with VERA. *Publ. Astron. Soc. Jpn.* **2019**, *71*, 16. [CrossRef]
59. Matsuno, M.; Nakagawa, A.; Morita, A.; Kurayama, T.; Omodaka, T.; Nagayama, T.; Honma, M.; Shibata, K.M.; Ueno, Y.; Jike, T.; et al. Annual parallax measurement of the Mira variable star BX Camelopardalis with VERA. *Publ. Astron. Soc. Jpn.* **2020**, *72*, 56. [CrossRef]
60. Lindegren, L.; Hernández, J.; Bombrun, A.; Klioner, S.; Bastian, U.; Ramos-Lerate, M.; de Torres, A.; Steidelmüller, H.; Stephenson, C.; Hobbs, D.; et al. Gaia Data Release 2. The astrometric solution. *Astrophys. Galaxies* **2018**, *616*, A2. [CrossRef]
61. Riess, A.G.; Casertano, S.; Yuan, W.; Macri, L.; Bucciarelli, B.; Lattanzi, M.G.; MacKenty, J.W.; Bowers, J.B.; Zheng, W.; Filippenko, A.V.; et al. Milky Way Cepheid Standards for Measuring Cosmic Distances and Application to Gaia DR2: Implications for the Hubble Constant. *Astrophys. J.* **2018**, *861*, 126. [CrossRef]
62. Zinn, J.C.; Pinsonneault, M.H.; Huber, D.; Stello, D. Confirmation of the Gaia DR2 Parallax Zero-point Offset Using Asteroseismology and Spectroscopy in the Kepler Field. *Astrophys. J.* **2019**, *878*, 136. [CrossRef]
63. Schönrich, R.; McMillan, P.; Eyer, L. Distances and parallax bias in Gaia DR2. *Mon. Not. RAS* **2019**, *487*, 3568–3580. [CrossRef]
64. Xu, Y.; Hou, L.G.; Bian, S.B.; Hao, C.J.; Liu, D.J.; Li, J.J.; Li, Y.J. Local spiral structure based on the Gaia EDR3 parallaxes. *Astrophys. Galaxies* **2021**, *645*, L8. [CrossRef]
65. Weidner, C.; Vink, J.S. The masses, and the mass discrepancy of O-type stars. *Astrophys. Galaxies* **2010**, *524*, A98. [CrossRef]
66. Xu, Y.; Hou, L.G.; Wu, Y.W. The spiral structure of the Milky Way. *Res. Astron. Astrophys.* **2018**, *18*, 146. [CrossRef]
67. Weaver, H.; Williams, D.R.W. The Berkeley low-latitude survey of neutral hydrogen Part I. Profiles. *Astron. Astrophys. Rev.* **1973**, *8*, 1.
68. Weaver, H. Some Aspects of Galactic Structure Derived from the Berkeley Low Latitude Survey of Neutral Hydrogen (invited Paper). In *Galactic Radio Astronomy*; Kerr, F.J., Simonson, S.C., Eds.; D. Reidel Pub. Co.: Dordrecht, The Netherlands; Boston, MA, USA, 1974; Volume 60, p. 573.
69. Cohen, R.S.; Cong, H.; Dame, T.M.; Thaddeus, P. Molecular clouds and galactic spiral structure. *Astrophys. J. Lett.* **1980**, *239*, L53–L56. [CrossRef]
70. Dame, T.M.; Hartmann, D.; Thaddeus, P. The Milky Way in Molecular Clouds: A New Complete CO Survey. *Astrophys. J.* **2001**, *547*, 792–813. [CrossRef]
71. Reid, M.J.; Dame, T.M.; Menten, K.M.; Brunthaler, A. A Parallax-based Distance Estimator for Spiral Arm Sources. *Astrophys. J.* **2016**, *823*, 77. [CrossRef]
72. Honig, Z.N.; Reid, M.J. Characteristics of Spiral Arms in Late-type Galaxies. *Astrophys. J.* **2015**, *800*, 53. [CrossRef]
73. Xu, Y.; Bian, S.B.; Reid, M.J.; Li, J.J.; Menten, K.M.; Dame, T.M.; Zhang, B.; Brunthaler, A.; Wu, Y.W.; Moscadelli, L.; et al. Trigonometric Parallaxes of Four Star-forming Regions in the Distant Inner Galaxy. *Astrophys. J. Suppl.* **2021**, *253*, 1. [CrossRef]
74. Wegg, C.; Gerhard, O.; Portail, M. The structure of the Milky Way's bar outside the bulge. *Mon. Not. RAS* **2015**, *450*, 4050–4069. [CrossRef]

75. May, J.; Bronfman, L.; Alvarez, H.; Murphy, D.C.; Thaddeus, P. A deep CO survey of the third galactic quadrant. *Astron. Astrophys. Rev.* **1993**, *99*, 105–165.
76. Hachisuka, K.; Choi, Y.K.; Reid, M.J.; Brunthaler, A.; Menten, K.M.; Sanna, A.; Dame, T.M. Parallaxes of Star-forming Regions in the Outer Spiral Arm of the Milky Way. *Astrophys. J.* **2015**, *800*, 2. [CrossRef]
77. Sakai, N.; Nagayama, T.; Nakanishi, H.; Koide, N.; Kurayama, T.; Izumi, N.; Hirota, T.; Yoshida, T.; Shibata, K.M.; Honma, M. Vertical structure and kinematics of the Galactic outer disk. *Publ. Astron. Soc. Jpn.* **2020**, *72*, 53. [CrossRef]
78. Urquhart, J.S.; Busfield, A.L.; Hoare, M.G.; Lumsden, S.L.; Oudmaijer, R.D.; Moore, T.J.T.; Gibb, A.G.; Purcell, C.R.; Burton, M.G.; Marechal, L.J.L. The RMS survey. ^{13}CO observations of candidate massive YSOs in the southern Galactic plane. *Astrophys. Galaxies* **2007**, *474*, 891–901. [CrossRef]
79. Anderson, L.D.; Armentrout, W.P.; Luisi, M.; Bania, T.M.; Balser, D.S.; Wenger, T.V. A Green Bank Telescope Survey of Large Galactic H II Regions. *Astrophys. J. Suppl.* **2018**, *234*, 33. [CrossRef]
80. Zhang, B.; Reid, M.J.; Zhang, L.; Wu, Y.; Hu, B.; Sakai, N.; Menten, K.M.; Zheng, X.; Brunthaler, A.; Dame, T.M.; et al. Parallaxes for Star-forming Regions in the Inner Perseus Spiral Arm. *Astron. J.* **2019**, *157*, 200. [CrossRef]
81. Choi, Y.K.; Hachisuka, K.; Reid, M.J.; Xu, Y.; Brunthaler, A.; Menten, K.M.; Dame, T.M. Trigonometric Parallaxes of Star Forming Regions in the Perseus Spiral Arm. *Astrophys. J.* **2014**, *790*, 99. [CrossRef]
82. Sakai, N.; Reid, M.J.; Menten, K.M.; Brunthaler, A.; Dame, T.M. Noncircular Motions in the Outer Perseus Spiral Arm. *Astrophys. J.* **2019**, *876*, 30. [CrossRef]
83. Roberts, W.W. Large-Scale Shock Formation in Spiral Galaxies and its Implications on Star Formation. *Astrophys. J.* **1969**, *158*, 123. [CrossRef]
84. Roberts, W.W., Jr. Application of the Density-Wave Theory of Spiral Structure: Shock Formation Along the Perseus Arm. *Astrophys. J.* **1972**, *173*, 259. [CrossRef]
85. Bobylev, V.V.; Bajkova, A.T. The Milky Way spiral structure parameters from data on masers and selected open clusters. *Mon. Not. RAS* **2014**, *437*, 1549–1553. [CrossRef]
86. Xu, Y.; Reid, M.; Dame, T.; Menten, K.; Sakai, N.; Li, J.; Brunthaler, A.; Moscadelli, L.; Zhang, B.; Zheng, X. The local spiral structure of the Milky Way. *Sci. Adv.* **2016**, *2*, e1600878. [CrossRef]
87. Xu, Y.; Li, J.J.; Reid, M.J.; Menten, K.M.; Zheng, X.W.; Brunthaler, A.; Moscadelli, L.; Dame, T.M.; Zhang, B. On the Nature of the Local Spiral Arm of the Milky Way. *Astrophys. J.* **2013**, *769*, 15. [CrossRef]
88. Yuan, C. Application of the Densiity-Wave Theory to the Spiral Structure of the Milky way System. I. Systematic Motion of Neutral Hydrogen. *Astrophys. J.* **1969**, *158*, 871. [CrossRef]
89. Wu, Y.W.; Sato, M.; Reid, M.J.; Moscadelli, L.; Zhang, B.; Xu, Y.; Brunthaler, A.; Menten, K.M.; Dame, T.M.; Zheng, X.W. Trigonometric parallaxes of star-forming regions in the Sagittarius spiral arm. *Astrophys. Galaxies* **2014**, *566*, A17. [CrossRef]
90. Bitran, M.; Alvarez, H.; Bronfman, L.; May, J.; Thaddeus, P. A large scale CO survey of the Galactic center region. *Astron. Astrophys. Rev.* **1997**, *125*, 99–138. [CrossRef]
91. Zhang, B.; Moscadelli, L.; Sato, M.; Reid, M.J.; Menten, K.M.; Zheng, X.W.; Brunthaler, A.; Dame, T.M.; Xu, Y.; Immer, K. The Parallax of W43: a Massive Star-forming Complex near the Galactic Bar. *Astrophys. J.* **2014**, *781*, 89. [CrossRef]
92. Sato, M.; Wu, Y.W.; Immer, K.; Zhang, B.; Sanna, A.; Reid, M.J.; Dame, T.M.; Brunthaler, A.; Menten, K.M. Trigonometric Parallaxes of Star Forming Regions in the Scutum Spiral Arm. *Astrophys. J.* **2014**, *793*, 72. [CrossRef]
93. Immer, K.; Li, J.; Quiroga-Nuñez, L.H.; Reid, M.J.; Zhang, B.; Moscadelli, L.; Rygl, K.L.J. Anomalous peculiar motions of high-mass young stars in the Scutum spiral arm. *Astrophys. Galaxies* **2019**, *632*, A123. [CrossRef]
94. Davis, B.L.; Berrier, J.C.; Shields, D.W.; Kennefick, J.; Kennefick, D.; Seigar, M.S.; Lacy, C.H.S.; Puerari, I. Measurement of Galactic Logarithmic Spiral Arm Pitch Angle Using Two-dimensional Fast Fourier Transform Decomposition. *Astrophys. J. Suppl.* **2012**, *199*, 33. [CrossRef]
95. Sakai, N.; Honma, M.; Nakanishi, H.; Sakanoue, H.; Kurayama, T.; Shibata, K.M.; Shizugami, M. Outer Rotation Curve of the Galaxy with VERA I: Trigonometric Parallax of IRAS 05168+3634. *Publ. Astron. Soc. Jpn.* **2012**, *64*, 108. [CrossRef]
96. Honma, M.; Nagayama, T.; Ando, K.; Bushimata, T.; Choi, Y.K.; Handa, T.; Hirota, T.; Imai, H.; Jike, T.; Kim, M.K.; et al. Fundamental Parameters of the Milky Way Galaxy Based on VLBI astrometry. *Publ. Astron. Soc. Jpn.* **2012**, *64*, 136. [CrossRef]
97. Persic, M.; Salucci, P.; Stel, F. The universal rotation curve of spiral galaxies— I. The dark matter connection. *Mon. Not. RAS* **1996**, *281*, 27–47. [CrossRef]
98. Schönrich, R.; Binney, J.; Dehnen, W. Local kinematics and the local standard of rest. *Mon. Not. RAS* **2010**, *403*, 1829–1833. [CrossRef]
99. Quiroga-Nuñez, L.H.; van Langevelde, H.J.; Reid, M.J.; Green, J.A. Simulated Galactic methanol maser distribution to constrain Milky Way parameters. *Astrophys. Galaxies* **2017**, *604*, A72. [CrossRef]
100. Reed, B.C. Catalog of Galactic OB Stars. *Astron. J.* **2003**, *125*, 2531–2533. [CrossRef]
101. Bobylev, V.V.; Krisanova, O.I.; Bajkova, A.T. Study of the Galactic Rotation Based on Masers and Radio Stars with VLBI Measurements of Their Parallaxes. *Astron. Lett.* **2020**, *46*, 439–448. [CrossRef]
102. Ortiz-León, G.N.; Menten, K.M.; Kamiński, T.; Brunthaler, A.; Reid, M.J.; Tylenda, R. SiO maser astrometry of the red transient V838 Monocerotis. *Astrophys. Galaxies* **2020**, *638*, A17. [CrossRef]
103. Leung, H.W.; Bovy, J.; Mackereth, J.T.; Hunt, J.A.S.; Lane, R.R.; Wilson, J.C. A direct measurement of the distance to the Galactic center using the kinematics of bar stars. *arXiv* **2022**, arXiv:2204.12551.

104. Abdurro'uf; Accetta, K.; Aerts, C.; Silva Aguirre, V.; Ahumada, R.; Ajgaonkar, N.; Filiz Ak, N.; Alam, S.; Allende Prieto, C.; Almeida, A.; et al. The Seventeenth Data Release of the Sloan Digital Sky Surveys: Complete Release of MaNGA, MaStar, and APOGEE-2 Data. *Astrophys. J. Suppl.* **2022**, *259*, 35. [CrossRef]
105. Xu, Y.; Bian, S.B.; Reid, M.J.; Li, J.J.; Zhang, B.; Yan, Q.Z.; Dame, T.M.; Menten, K.M.; He, Z.H.; Liao, S.L.; et al. A comparison of the local spiral structure from Gaia DR2 and VLBI maser parallaxes. *Astrophys. Galaxies* **2018**, *616*, L15. [CrossRef]
106. Groenewegen, M.A.T.; Udalski, A.; Bono, G. The distance to the Galactic centre based on Population II Cepheids and RR Lyrae stars. *Astrophys. Galaxies* **2008**, *481*, 441–448. [CrossRef]
107. Schönrich, R. Galactic rotation and solar motion from stellar kinematics. *Mon. Not. RAS* **2012**, *427*, 274–287. [CrossRef]
108. Do, T.; Hees, A.; Ghez, A.; Martinez, G.D.; Chu, D.S.; Jia, S.; Sakai, S.; Lu, J.R.; Gautam, A.K.; O'Neil, K.K.; et al. Relativistic redshift of the star S0-2 orbiting the Galactic Center supermassive black hole. *Science* **2019**, *365*, 664–668. [CrossRef]
109. Abuter, R. et al. [Gravity Collaboration]. Improved GRAVITY astrometric accuracy from modeling optical aberrations. *Astrophys. Galaxies* **2021**, *647*, A59. [CrossRef]
110. Mróz, P.; Udalski, A.; Skowron, D.M.; Skowron, J.; Soszyński, I.; Pietrukowicz, P.; Szymański, M.K.; Poleski, R.; Kozłowski, S.; Ulaczyk, K. Rotation Curve of the Milky Way from Classical Cepheids. *Astrophys. J. Lett.* **2019**, *870*, L10. [CrossRef]
111. Ablimit, I.; Zhao, G.; Flynn, C.; Bird, S.A. The Rotation Curve, Mass Distribution, and Dark Matter Content of the Milky Way from Classical Cepheids. *Astrophys. J. Lett.* **2020**, *895*, L12. [CrossRef]
112. Eilers, A.C.; Hogg, D.W.; Rix, H.W.; Ness, M.K. The Circular Velocity Curve of the Milky Way from 5 to 25 kpc. *Astrophys. J.* **2019**, *871*, 120. [CrossRef]
113. Bobylev, V.V.; Bajkova, A.T. Galaxy Rotation Parameters from OB2 Stars with Proper Motions and Parallaxes from the Gaia EDR3 Catalog. *Astron. Rep.* **2022**, *66*, 269–277. [CrossRef]
114. Reid, M.J.; Brunthaler, A. The Proper Motion of Sagittarius A*. III. The Case for a Supermassive Black Hole. *Astrophys. J.* **2020**, *892*, 39. [CrossRef]
115. Skowron, D.M.; Skowron, J.; Mróz, P.; Udalski, A.; Pietrukowicz, P.; Soszyński, I.; Szymański, M.K.; Poleski, R.; Kozłowski, S.; Ulaczyk, K.; et al. A three-dimensional map of the Milky Way using classical Cepheid variable stars. *Science* **2019**, *365*, 478–482. [CrossRef]
116. Majewski, S.R.; Schiavon, R.P.; Frinchaboy, P.M.; Allende Prieto, C.; Barkhouser, R.; Bizyaev, D.; Blank, B.; Brunner, S.; Burton, A.; Carrera, R.; et al. The Apache Point Observatory Galactic Evolution Experiment (APOGEE). *Astron. J.* **2017**, *154*, 94. [CrossRef]
117. Skrutskie, M.F.; Cutri, R.M.; Stiening, R.; Weinberg, M.D.; Schneider, S.; Carpenter, J.M.; Beichman, C.; Capps, R.; Chester, T.; Elias, J.; et al. The Two Micron All Sky Survey (2MASS). *Astron. J.* **2006**, *131*, 1163–1183. [CrossRef]
118. Wright, E.L.; Eisenhardt, P.R.M.; Mainzer, A.K.; Ressler, M.E.; Cutri, R.M.; Jarrett, T.; Kirkpatrick, J.D.; Padgett, D.; McMillan, R.S.; Skrutskie, M.; et al. The Wide-field Infrared Survey Explorer (WISE): Mission Description and Initial On-orbit Performance. *Astron. J.* **2010**, *140*, 1868–1881. [CrossRef]
119. Bobylev, V.V.; Bajkova, A.T. The z distribution of hydrogen clouds and masers with kinematic distances. *Astron. Lett.* **2016**, *42*, 182–192. [CrossRef]
120. Anderson, L.D.; Wenger, T.V.; Armentrout, W.P.; Balser, D.S.; Bania, T.M. A Galactic Plane Defined by the Milky Way H II Region Distribution. *Astrophys. J.* **2019**, *871*, 145. [CrossRef]
121. Minniti, J.H.; Zoccali, M.; Rojas-Arriagada, A.; Minniti, D.; Sbordone, L.; Contreras Ramos, R.; Braga, V.F.; Catelan, M.; Duffau, S.; Gieren, W.; et al. Using classical Cepheids to study the far side of the Milky Way disk. II. The spiral structure in the first and fourth Galactic quadrants. *Astrophys. Galaxies* **2021**, *654*, A138. [CrossRef]
122. Gómez, F.A.; Minchev, I.; O'Shea, B.W.; Beers, T.C.; Bullock, J.S.; Purcell, C.W. Vertical density waves in the Milky Way disc induced by the Sagittarius dwarf galaxy. *Mon. Not. RAS* **2013**, *429*, 159–164. [CrossRef]
123. Green, J.; van Langevelde, H.; Brunthaler, A.; Ellingsen, S.; Imai, H.; Vlemmings, W.; Reid, M.; Richards, A. *Maser Astrometry with VLBI and the SKA*; Proceedings of Science: Trieste, Italy, 2015.
124. Rioja, M.J.; Dodson, R. Precise radio astrometry and new developments for the next-generation of instruments. *Astron. Astrophys. Rev.* **2020**, *28*, 6. [CrossRef]
125. Hyland, L.J.; Reid, M.J.; Ellingsen, S.P.; Rioja, M.J.; Dodson, R.; Orosz, G.; Masson, C.R.; MacCallum, J. Inverse Multiview I: Multi-Calibrator inverse phase referencing for Microarcsecond VLBI Astrometry. *arXiv* **2022**, arXiv:2205.00092.